A vorticity-divergence view of internal wave generation by tropical cyclones: insights from Super Typhoon Mangkhut

Noel G. Brizuela[1,1], T. M. Shaun Johnston[2,2], Matthew H Alford[2,2], Olivier Asselin[3,3], Daniel L. Rudnick[2,2], Jim Moum[4,4], Elizabeth J Thompson[5,5], Shuguang Wang[6,6], and Chia-Ying Lee[7,7]

[1]University of California, San Diego
[2]Scripps Institution of Oceanography
[3]Scripps Institution of Oceanography, UC San Diego
[4]Oregon State University
[5]NOAA Earth System Research Lab
[6]Nanjing University
[7]Lamont Doherty Earth Observatory

November 30, 2022

Abstract

Tropical cyclones (TCs) are powered by heat fluxes across the air-sea interface, which are in turn influenced by subsurface physical processes that can modulate storm intensity. Here, we use data from 6 profiling floats to recreate 3D fields of temperature (T), salinity (S), and velocity around Super Typhoon Mangkhut (western North Pacific, September 2018). Observational estimates of vorticity (ζ) and divergence (Γ) agree with output from a 3D coupled model, while their relation to vertical velocities is explained by a linear theoretical statement of inertial pumping. Under this framework, inertial pumping is described as a linear coupling between ζ and Γ, whose cycles cause periodic displacements in the ocean thermocline and generate near-inertial waves (NIWs). Vertical profiles of T and S show gradual mixing of the upper ocean with diffusivities as high as $\varkappa$˜10ˆ-1 mˆ2 sˆ-1, which caused an asymmetric cold wake of sea surface temperature (SST). We estimate that rain layer destruction used ˜ 10% of energy used for mixing near the TC track, therefore inhibiting SST cooling. Lastly, watermass transformation analyses suggest that $\varkappa >$ 3x10ˆ-3 mˆ2 sˆ-1 above ˜110 m depth and up to 600 km behind the TC. These analyses provide an observational summary of the ocean response to TCs, demonstrate some advantages of ζ and Γ for the study of internal wave fields, and provide conceptual clarity on the mechanisms that lead to NIW generation behind TCs.

A vorticity-divergence view of internal wave generation by tropical cyclones: insights from Super Typhoon Mangkhut

Noel G. Brizuela[1], T. M. Shaun Johnston[1], Matthew H. Alford[1], Olivier Asselin[1], Daniel L. Rudnick[1], James N. Moum[2], Elizabeth J. Thompson[3], Shuguang Wang[4], Chia-Ying Lee[5]

[1]Scripps Institution of Oceanography, University of California, San Diego, La Jolla, CA, USA
[2]College of Earth, Ocean and Atmospheric Science, Oregon State University, Corvallis, OR, USA
[3]NOAA Physical Sciences Laboratory, Boulder, CO, USA
[4]School of Atmospheric Sciences, Nanjing University, Nanjing 210023, China
[5]Lamont-Doherty Earth Observatory, Columbia University, New York, NY, USA

Key Points:

- Float data, linear theory, and 3D model show that coupling between vorticity and divergence controls inertial pumping under tropical cyclone
- Asymmetric sea surface cooling 1.2ºC dominated by mixing and modulated by rainfall, which used 10% of turbulent energy during forced stage
- Estimates of turbulent diffusivity explain sea surface cooling rates 0.1 °C hr^{-1} under typhoon eye and thermocline mixing in its wake

Corresponding author: Noel G. Brizuela, nogutier@ucsd.edu

Abstract

Tropical cyclones (TCs) are powered by heat fluxes across the air-sea interface, which are in turn influenced by subsurface physical processes that can modulate storm intensity. Here, we use data from 6 profiling floats to recreate 3D fields of temperature (T), salinity (S), and velocity around Super Typhoon Mangkhut (western North Pacific, September 2018). Observational estimates of vorticity (ζ) and divergence (Γ) agree with output from a 3D coupled model, while their relation to vertical velocities is explained by a linear theoretical statement of inertial pumping. Under this framework, inertial pumping is described as a linear coupling between ζ and Γ, whose cycles cause periodic displacements in the ocean thermocline and generate near-inertial waves (NIWs). Vertical profiles of T and S show gradual mixing of the upper ocean with diffusivities as high as $\kappa \sim 10^{-1}$ m^2 s^{-1}, which caused an asymmetric cold wake of sea surface temperature (SST). We estimate that rain layer destruction used $\sim 10\%$ of energy used for mixing near the TC track, therefore inhibiting SST cooling. Lastly, watermass transformation analyses suggest that $\kappa > 3{\times}10^{-3}$ m^2 s^{-1} above $\sim$110 m depth and up to 600 km behind the TC. These analyses provide an observational summary of the ocean response to TCs, demonstrate some advantages of ζ and Γ for the study of internal wave fields, and provide conceptual clarity on the mechanisms that lead to NIW generation behind TCs.

Plain Language Summary

Near-inertial internal waves (NIWs) are generated by winds and lead to oscillations in the internal structure of ocean currents and stratification. Turbulence induced by the vertical current shear in these waves is key to sustain the upper ocean stratification and circulation. In this study, we use data from 6 autonomous floats deployed ahead of Super Typhoon Mangkhut to reconstruct the ocean's 3D response. Reconstructed velocity fields agree with output from a coupled 3D model. Linear equations for vorticity and divergence are used to explain patterns in measured currents and NIW generation, as inertial coupling between wind-driven vorticity and divergence pumps the stratified ocean interior. Measurements of temperature and salinity detail how turbulent stirring mixed rainfall and thermocline waters into the upper ocean. Our analyses indicate that turbulent mixing rates are greatest within 100 km of the typhoon eye but remain elevated hundreds of kilometers behind Mangkhut. Theory and observations presented here provide a comprehensive view of the ocean response to fast-moving, high-intensity tropical cyclones.

1 Introduction

Wind-powered currents that rotate near the inertial frequency (f) dominate upper ocean dynamics behind fast-moving tropical cyclones (TCs). On the right (left) side of Northern (Southern) hemisphere storms, transient winds amplify the magnitude of inertial currents, but suppress them on the opposite side (Chang & Anthes, 1978; Price, 1981). Horizontal convergence and divergence associated with these currents lead to inertial pumping of the mixed layer (ML) base. This process transfers ML momentum into near-inertial internal waves (NIWs) that later propagate across the ML base and into the thermocline (Price, 1983; Gill, 1984; D'Asaro et al., 2007; Sanford et al., 2011; Johnston et al., 2021). Although inertial pumping and its interactions with background ocean motions are well understood (Balmforth et al., 1998; Whitt & Thomas, 2015; Thomas et al., 2020), general approaches that help understand links between storm morphology and resulting patterns of NIW generation are still lacking.

Turbulence and advection associated with near-inertial motions help redistribute heat across subsurface reservoirs. Notably, shear-driven turbulence at the ML base cools

the sea surface temperature (SST) during and shortly after TC passage, reducing subsequent heat fluxes to the atmosphere and helping modulate storm intensity (Emanuel, 1999; Glenn et al., 2016). Although SST cooling by turbulent mixing typically stops after TC passage, the subsurface effects of mixing in TC wakes over longer timescales remain unclear. However, the final vertical distribution of temperature anomalies that result from this mixing determines a TC's impact on ocean heat uptake and transport (Jansen et al., 2010). Therefore, in situ measurements are necessary to estimate the magnitude of κ in TC wakes and assess the reliability of SST-based parameterizations of TC-driven mixing (Sriver & Huber, 2007; Korty et al., 2008).

In this article, we use data from six profiling floats (Johnston et al., 2020, 2021) to reconstruct the 3D fields of temperature (T), salinity (S), and currents (u, v, w) beneath Super Typhoon Mangkhut (Fig. 1). Our treatment of the data is validated using output from a coupled 3D ocean-atmosphere model of Mangkhut. Under the assumption that the upper ocean response to TC forcing approaches a steady state when viewed in storm-following coordinates (Geisler, 1970), we diagnose the roles of upwelling, advection, and mixing in the redistribution of subsurface heat and rainfall inputs. Float velocity data are used to validate linear theory results showing that upwelling and NIW generation under TCs result from the coupling of ML vorticity ($\zeta \equiv \frac{\partial v}{\partial x} - \frac{\partial u}{\partial y}$) and divergence ($\Gamma \equiv \frac{\partial u}{\partial x} + \frac{\partial v}{\partial y}$) by Earth's rotation. As explained below, this coupling is equivalent to the horizontal rotation of near-inertial currents.

Section 2 describes our data and processing methods including details about the 3D model used for validation. Section 3 lays out the linear theory of upwelling and NIW generation under TCs and reformulates standard ML dynamics in terms of ζ and Γ to demonstrate their inertial coupling. Section 4 presents observational and modelled maps of (u, v) to verify relations between wind forcing, vorticity, divergence and NIW generation. Indirect evidence of turbulent mixing under Mangkhut is presented using float measurements of T and S in Section 5. A discussion of our methods and results is presented in Section 6, while conclusions are given in Section 7.

2 Data and Methods

Super Typhoon Mangkhut originated on September 7, 2018 as a tropical depression in the central Pacific Ocean and later intensified as it moved westwards into the Philippine Sea. Between September 11 and 15, it sustained maximum 1-minute wind speeds above 70 m s^{-1}, equivalent to a category 5 hurricane. Throughout this period, SOLO-II floats (Davis et al., 2001) sampled the ocean response under the TC (Fig. 1b). The combination of Mangkhut's long lifespan and elevated intensity put it among the 0.5% most powerful tropical storms on record (Fig. 1c, Emanuel 2005). As it travelled through the Philippine and South China Seas, Mangkhut caused significant damage and loss of life in the Philippines, Guam, Taiwan, Hong Kong, and China (Wamsley, 2018).

Upon deployment, the floats modified their buoyancy to dive up to 200 m depth and back to the surface at intervals < 50 minutes. While doing so, they upward obtained profiles of T and S, and drifted westward with the North-Equatorial Current at ~ 0.18 m s^{-1} (Fig. 2a, Johnston et al. 2020). Because floats record their coordinates at the beginning and end of every dive cycle, their Global Positioning System data yields two estimates of horizontal velocity (Fig. 2b). $\mathbf{u}_{mean}$ is the depth-mean current over the profiling range and is calculated using the difference between the start and end locations of individual dives. Surface estimates $\mathbf{u}_{surf}$, which are subject to wave motion and windage, are calculated using the drift between consecutive dives, when floats remain at the surface for ~ 5 minutes while they transfer data via Iridium satellite.

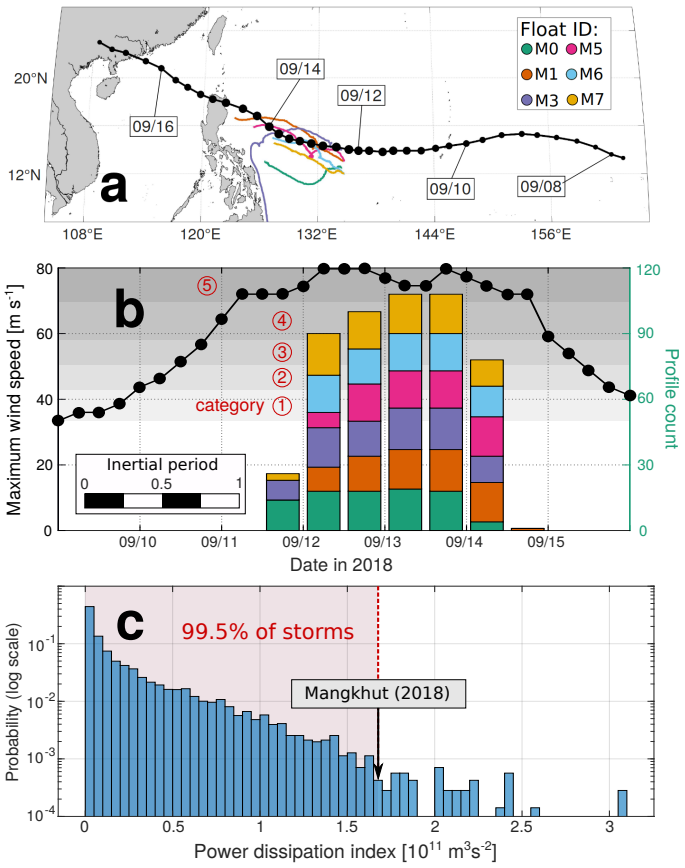

Figure 1. TC overview. (**a**) Best track data from the Joint Typhoon Warning Center shown in black and float trajectories are in colors. (**b**) Maximum 1-minute sustained wind speed $|U_{10}|$ (dotted line, left axis) and histogram showing the time distribution of float measurements. Gray shading in shows the wind speed thresholds for Saffir-Simpson TC categories 1 ($|U_{10}| \leq 30$ m s^{-1}) to 5 ($|U_{10}| > 70$ m s^{-1}). (**c**) Probability distribution of power dissipation index estimated for >7000 storms puts Mangkhut among the 0.5% most powerful tropical storms in record.

Output from a coupled ocean-atmosphere model of Mangkhut is compared to dynamical insights derived from float velocity data. The coupled system uses the Weather Research and Forecast (WRF) model V3.8.1 (Skamarock et al., 2008) as its atmospheric component, while the ocean is represented by the Hybrid Coordinate Ocean Model V2.2 (HYCOM; Wallcraft et al. 2009). Horizontal grid spacing in HYCOM was 1/12° for 41 vertical layers (10 in the upper 50 m) and output was saved at 3 hour intervals. Chen & Curcic (2016) give an assessment of this coupled model's performance under North Atlantic TCs. Further details about the model configuration used for Mangkhut were given by Johnston et al. (2021).

Comparisons of model output against measured $\mathbf{u}_{surf}$ (Fig. 3) are indicative of both the accuracy of the simulation and that of float velocity estimates. Although qualitative agreement between both datasets is good, neither float nor model data in Fig. 3 should be regarded as ground truth for ocean conditions at a time and place. While $\mathbf{u}_{surf}$ may be biased by windage or wave motion, the model's atmospheric component lets Mangkhut evolve dynamically, such that the modelled track and intensity differ slightly from observations (Johnston et al., 2021). To account for this, model velocities $\vec{u}_{hycom}$ in Fig.

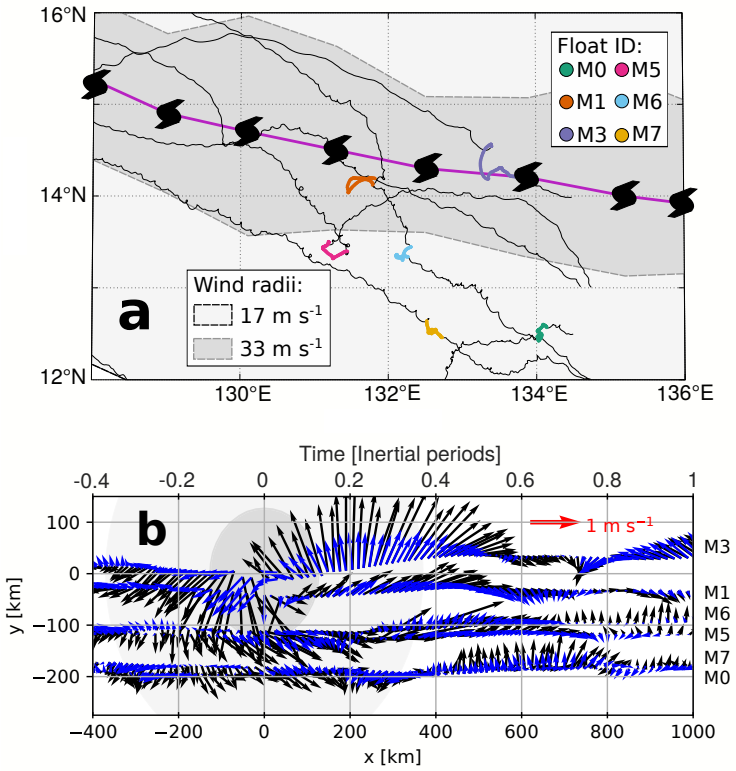

Figure 2. (**a**) 6-hourly JTWC best track data for Mangkhut (light purple). Black lines mark float trajectories, while the locations of vertical profiles used in this study are highlighted in colors. (**b**) Plane view of $\mathbf{u}_{surf}$ (black) and $\mathbf{u}_{mean}$ (blue), with x and y components scaled equally to show the true direction of currents in storm-following coordinates (x, y).

3 were taken from the average location of each float within 24 h of TC passage. As described next, objective mapping of float data onto storm-following coordinates provides a more meaningful representation of of ML dynamics under Mangkhut than pointwise comparisons in Fig. 3.

2.1 3D reconstruction of the ocean response

Best track data for Mangkhut from the Joint Typhoon Warning Center (JTWC) was linearly interpolated to the times of float data, which were then reorganized in storm-following coordinates (x, y) (Fig. 2b). Positive values of x denote regions behind the storm eye, while $y > 0$ indicates locations right of the TC track. Likewise, $\mathbf{u}_{surf}$ and $\mathbf{u}_{mean}$ were rotated such that u and v represent along-track and cross-track velocities respectively. Plots in (x, y) use the equivalent time $t = x/U_{storm}$ ($U_{storm} = 6.2$ m s^{-1}) to preserve information about temporal variability that has been mapped onto x. Time scaling $t\frac{f}{2\pi}$ uses the inertial period $\frac{2\pi}{f}$ at 15.54°N ($\sim$ 45 hr) such that one inertial period in t corresponds to $U_{storm}\frac{2\pi}{f}$ =1000 km in x (Fig. 2b).

Despite the fact that each float effectively sampled different parts of the storm at different times (Fig. 2a), both $\mathbf{u}_{surf}$ and $\mathbf{u}_{mean}$ line up with $v < 0$ ($v > 0$) for $x < 0$ ($x > 0$) and later rotate in the clockwise sense in the TC wake. Such similarities in measurements made by different floats at different times in Fig. 2b suggest that the ocean response was steady within the TC-following (x, y) coordinates (Geisler, 1970). To best

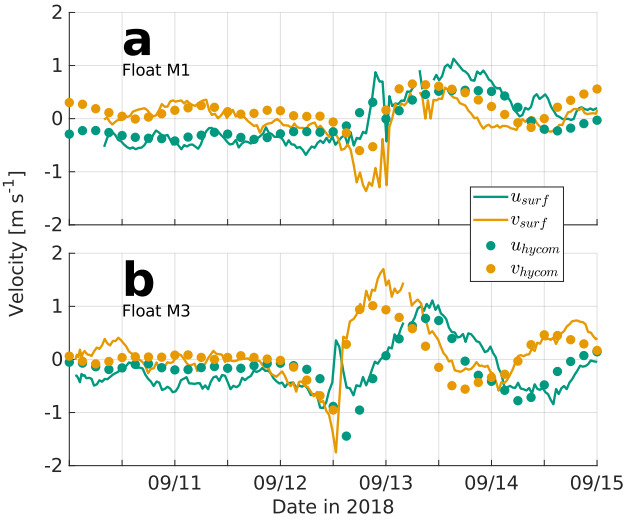

Figure 3. Model-observation comparison of upper ocean velocities. ML velocities $\vec{u}_{hycom}$ (circles) at fixed locations in the coupled 3D model are compared against measurements $\vec{u}_{surf}$ (solid lines) from floats (**a**) M1 and (**b**) M3.

exploit the spatiotemporal information embedded in float data, we used objective mapping (Davis, 1985; Le Traon et al., 1998) with a Gaussian decorrelation scale of 150 km to horizontally interpolate measurements $\mathbf{u}_{surf}$, $\mathbf{u}_{mean}$, T, and S. The signal-to-noise ratio for objective mapping was set to 10, and areas where the estimated mean square error of interpolated fields is greater than 7.5% of signal variance have been masked out in plots.

To reconstruct 3D patterns in T and S, we stacked 2D maps at 5 m intervals, thus producing $T^*(x, y, z)$ and $S^*(x, y, z)$. Here, the star * denotes objectively mapped variables. Although vertical variations in u, v were not measured directly, we use differences between $\mathbf{u}^*_{surf}$ and $\mathbf{u}^*_{mean}$ to separate the ML flow from the less energetic ocean below (Johnston et al., 2021). More precisely, we assume that depth-dependence at each location (x, y) is given by

$$\mathbf{u}^*(x,y,z) = \begin{cases} \mathbf{u}^*_{surf} & z \geq -h \\ \mathbf{u}^*_{surf} + \left\langle \frac{\partial \mathbf{u}}{\partial z} \right\rangle (z-h) & -h > z > -h-l \\ \mathbf{u}^*_{surf} + \left\langle \frac{\partial \mathbf{u}}{\partial z} \right\rangle l & -h-l \geq z \geq -H. \end{cases} \tag{1}$$

The piecewise function (1) includes two layers of depth-constant velocity and a sheared transition layer between them. Flow in the uppermost layer, which spans the depth of the ML $-h < z \leq 0$, is given by $\mathbf{u}^*_{surf}$. Here, h is defined as the depth at which T^* is 0.2 °C colder than it is at 20 m depth; this helps avoid transient effects of diurnal warm layers and rain layers, whose timescale of dynamical significance under intense wind forcing is much shorter than that of near-inertial motions (E. J. Thompson et al., 2019; Hughes et al., 2020). Below $z = -h$, we assume a transition layer of thickness l and constant shear

$$\left\langle \frac{\partial \mathbf{u}}{\partial z} \right\rangle = 2H \frac{\mathbf{u}^*_{surf} - \mathbf{u}^*_{mean}}{[l^2 + 2l(H-l-h)]}. \tag{2}$$

This transition layer is set by the vertical penetration of wind-driven turbulent momentum, which determines the depth at which $\mathbf{u}$ no longer behaves like a slab (Turner & Kraus, 1967; Pollard et al., 1973). In reality, the transition layer thickness can vary considerably and is seen as a stratification and shear maximum below the ML base (Johnston & Rudnick, 2009). However, vigorous mixing and internal wave strain behind Mangkhut makes it such that a transition layer cannot be reliably identified in profiles of T and S at many locations; therefore, we set a constant thickness $l = 30$ m. However, Lastly, the third and deepest layer extends down to $H = 180\,\mathrm{m}$ and has velocities $\mathbf{u}^*_{surf} + \left\langle \frac{\partial \mathbf{u}}{\partial z} \right\rangle l$. This construction makes the depth-mean of $\mathbf{u}^*$ between $z = 0$ and $z = -H$ equal to $\mathbf{u}^*_{mean}$.

Concentrating $\left\langle \frac{\partial \mathbf{u}}{\partial z} \right\rangle$ within a transition layer captures some of the main features of wind-forced currents. Thus, equations (1) and (2) yield an idealized 3D velocity field constrained by float velocity estimates and previous knowledge of the baroclinic response to TC forcing. However, it should be noted that high baroclinic modes that cannot be represented by equation (1).

To finalize the reconstruction of 3D flows beneath Mangkhut from float measurements, we impose a condition of adiabatic continuity to obtain $\frac{\partial w^*}{\partial z} = -\frac{\partial u^*}{\partial x} - \frac{\partial v^*}{\partial y}$. Furthermore, we assume a rigid lid so that $w^*(z = 0)$ vanishes and the vertical velocity is

$$w^*(x, y, z) = \int_0^z \left(\frac{\partial u^*}{\partial x} + \frac{\partial v^*}{\partial y} \right) dz'. \tag{3}$$

Before showing the interpolated fields T^*, S^*, u^*, v^*, w^*, we must emphasize that (1) the decorrelation scale $L = 150$ km suppresses high-frequency features in the observations, and (2) caution is warranted when interpreting results near the edge of the objective maps.

2.2 Thorpe scale estimates of turbulence

Vertical profiles of T and S taken at 1 Hz (vertical resolution ~ 0.2 m) were used to compute in situ density (ρ). These allowed us to derive Thorpe scale estimates (Thorpe, 1977) of the turbulent dissipation rate (ε) and diffusivity (κ) within unstable overturns where $\frac{\partial \rho}{\partial z} > 0$. This method computes the vertical displacements d' necessary to reorder water parcels within a given overturn such that ρ increases with depth. This defines the Thorpe scale as $L_{Ti} = \sqrt{\langle d'^2 \rangle_i}$, where the brackets indicate averaging within an overturn i. Given this, ε was calculated as

$$\varepsilon_i = 0.64 L_{Ti}^2 \langle N \rangle_i^3. \tag{4}$$

Here, $\langle N \rangle_i$ is the mean buoyancy frequency calculated from the sorted profile of ρ. Next, we used the relation in Osborn (1980) to compute $\kappa_i = 0.2 \frac{\varepsilon_i}{\tilde{N}^2}$. Here, $\tilde{N}$ is the background buoyancy frequency from sorted profiles of ρ. With this, ε and κ were indirectly estimated for all overturns whose $L_{Ti} > 5$ m. This allows us to estimate the downward turbulent heat flux

$$J_{qi} = \rho_0 C_p \kappa_i \langle \frac{\partial T}{\partial z} \rangle_i. \tag{5}$$

Here, the constants are $\rho_0 = 1024$ kg m^{-3} and $C_p = 4000$ J kg^{-1} °C^{-1}. More details on the implementation, assumptions, and limitations of the Thorpe scale method can be found in Johnson & Garrett (2004); A. Thompson et al. (2007); Mater et al. (2015); Scotti (2015).

3 Mixed layer theory

In this section, we review the mechanisms of NIW generation by TCs and formulate linear ML dynamics. Instead of understanding ML motions using depth-averaged ML currents $\bar{\mathbf{u}} = (\bar{u}, \bar{v})$, we use their vorticity ($\zeta = \nabla \times \bar{\mathbf{u}}$) and divergence ($\Gamma = \nabla \cdot \bar{\mathbf{u}}$). This change of variables leads to a coupling between ζ and Γ that gives rise to inertial pumping and helps conceptualize NIW generation by TCs as a 1D rather than 3D process. By stating inertial pumping as a set of ordinary differential equations rather than partial, as done by Gill (1984), the spatiotemporal patterns of NIW generation are more easily related to the morphology of atmospheric forcing $\tau = (\tau_x, \tau_y)$.

The response of $\bar{\mathbf{u}}$ to τ in a ML of thickness h can be described using the linear slab model

$$\frac{\partial \bar{u}}{\partial t} = f\bar{v} + \frac{\tau_x}{\rho_0 h} - r\bar{u} \tag{6}$$

$$\frac{\partial \bar{v}}{\partial t} = -f\bar{u} + \frac{\tau_y}{\rho_0 h} - r\bar{v} \tag{7}$$

$$\frac{\partial h}{\partial t} + h\nabla \cdot \bar{\mathbf{u}} = W_e \tag{8}$$

Solutions to these equations, first used by Pollard & Millard (1970) to explain in situ measurements of $\bar{\mathbf{u}}$, feature a slowly-varying component that approximates an Ekman balance and inertial oscillations whose amplitude decays according to a damping coefficient (r). In order to resolve vertical velocities ($\frac{\partial h}{\partial t}$) at the ML base, we couple (6) and (7) to the continuity equation (8). Here, $W_e \geq 0$ is an entrainment rate used to represent ML deepening caused by turbulent mixing (Price, 1981).

Because our focus here is on NIW generation, equations (6)-(8) exclude forces that make negligible or secondary contributions to $\frac{\partial h}{\partial t}$. For example, barotropic flows develop in TC wakes (Shay & Chang, 1997), but the horizontal pressure gradients that drive them scale to make a negligible contribution to $\frac{\partial h}{\partial t}$ in baroclinic modes under TCs (Geisler, 1970; Gill, 1984; D'Asaro, 1989). Equations (6) and (7) ignore horizontal pressure gradients that result from gradients in both surface elevation and ML density. Similarly, solutions of $\frac{\partial h}{\partial t}$ that account for advective terms $\bar{\mathbf{u}} \cdot \nabla \bar{\mathbf{u}}$ and $\bar{\mathbf{u}} \cdot \nabla h$ under TCs (Price, 1981) show good agreement with the linear case solved by Geisler (1970), so the advective terms can be dropped.

When the ML base oscillates at frequencies slightly greater than f, periodic pumping of the ML base allows downward momentum transfer by NIWs (Price, 1983; Gill, 1984). The full baroclinic ocean response to TCs must be represented by coupling contiguous layers of increasing density through pressure gradients produced by interfacial displacements (Geisler, 1970; Price, 1983). Given that their focus is on the ML, equations (6) and (7) do not represent these thermocline processes explicitly. Rather, they use the empirical damping rate r to parameterize the gradual decay of ML momentum that results from them (Pollard & Millard, 1970; D'Asaro, 1989; D'Asaro et al., 1995).

The value of r is typically determined empirically to fit observations of $\overline{\mathbf{u}}$ (Pollard & Millard, 1970; Alford & Gregg, 2001; Guan et al., 2014), but is meant to represent the effects of internal wave propagation, nonlinearities, and turbulent dissipation alike. Previous studies have sought to derive scalings of the type $r^{-1} \sim E_{NIW}/F_{NIW}$, where E_{NIW} is the near-inertial energy and F_{NIW} is the corresponding energy flux (Gill, 1984). However, such derivations are necessarily incomplete and highly dependent on assumptions about the physical process by which NIWs develop horizontal gradients and their corresponding group velocity ($\mathbf{c_g}$). In the mid latitudes, this reduction of horizontal scales

is thought to depend on gradients in the mesoscale and planetary vorticity (Kunze, 1985; D'Asaro, 1989; Johnston et al., 2016; Asselin & Young, 2020; Thomas et al., 2020). In contrast, the spatial structure of TC winds imprints sharp gradients on upper ocean currents and thus allows for more rapid generation of NIWs (D'Asaro, 1989). To emphasize this point, we now consider the ML response to τ not in terms of $\bar{u}$ and $\bar{v}$, but their spatial gradients. The final aim here is to elucidate the drivers of inertial pumping in $\frac{\partial h}{\partial t}$, by which NIW energy propagates into the thermocline.

3.1 Dynamics of wind-forced gradients in the upper ocean

Below, we manipulate equations (6)-(8) to isolate the components that contribute to $\frac{\partial h}{\partial t}$ and thus generate NIWs. To do this, we calculate $\frac{\partial \zeta}{\partial t} = \nabla \times \frac{\partial \bar{\mathbf{u}}}{\partial t}$ and study its relation to $\frac{\partial \Gamma}{\partial t} = \nabla \cdot \frac{\partial \bar{\mathbf{u}}}{\partial t}$. Taking the curl and divergence of equations (6) and (7) thus yields an alternative representation of ML dynamics

$$\frac{\partial \zeta}{\partial t} = -f\Gamma + \frac{1}{\rho_0 h}\left(\nabla \times \tau - \frac{\tau}{h} \times \nabla h\right) - r\zeta \tag{9}$$

$$\frac{\partial \Gamma}{\partial t} = f\zeta + \frac{1}{\rho_0 h}\left(\nabla \cdot \tau - \frac{\tau}{h} \cdot \nabla h\right) - r\Gamma \tag{10}$$

$$\frac{\partial h}{\partial t} + h\Gamma = W_e. \tag{11}$$

This formalism does not explicitly include information about the magnitude and direction of currents. Instead, it uses the physical principles in equations (6)-(8) to resolve spatiotemporal patterns in $\frac{\partial h}{\partial t}$ that generate internal waves. While past studies have used ζ and Γ as the basis of fluid dynamical models (Névir & Sommer, 2009), these variables are particularly relevant to NIW generation and their interaction with background flows (Gill, 1984; Nagai et al., 2015; Whitt & Thomas, 2015). Furthermore, note that under axial-symmetric storms, $\nabla \cdot \tau$ and $\nabla \times \tau$ are fully determined by radial and tangential winds respectively. Thus, equations (9) and (10) show how these separate components of τ directly drive orthogonal but coupled modes of motion Γ and ζ in the ML.

In TC wakes, once winds cease to play a dominant role and the ML evolves freely, our diagnostic model (9)-(11) yields the three term balance

$$\frac{\partial \zeta}{\partial t} = -f\Gamma - r\zeta \tag{12}$$

$$\frac{\partial \Gamma}{\partial t} = f\zeta - r\Gamma. \tag{13}$$

This linear system of equations, a damped harmonic oscillator, produces inertial cycles in ζ and Γ with an exponential decay rate r. Inertial pumping arises directly from these cycles, which are simply a consequence of clockwise rotation in $\bar{\mathbf{u}}$. To visualize how equations (12) and (13) are an explicit statement of inertial pumping, we follow Gill (1984) and set $\tau = W_e = r = 0$ to consider an initial condition $(\zeta_i, \Gamma_i) = (c_i, 0)$ at time $t = t_i$, where $c_i > 0$. As illustrated in Fig. 4, equations (12) and (13) imply that inertial rotation of current vectors transforms ζ into Γ, and Γ into $-\zeta$ at time intervals $\sim \frac{\pi}{2f}$. Quadrature between ζ and Γ in this oscillatory mode means that NIW crests and troughs (maximum upward and downward displacements of the ML base) must be surrounded by anticyclonic and cyclonic inertial currents respectively (Fig. 4).

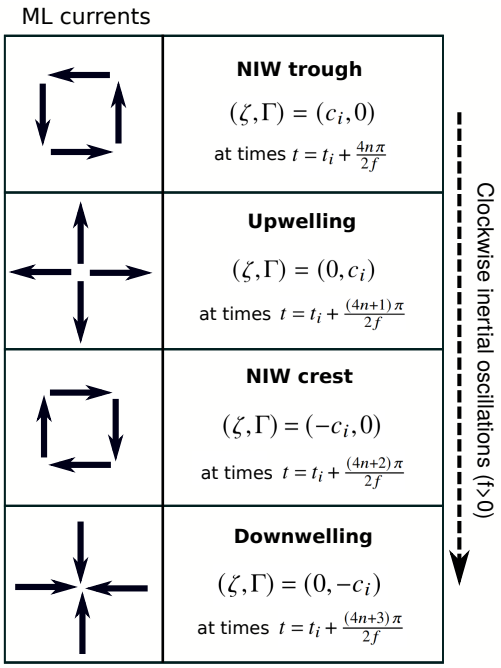

Figure 4. Successive rows illustrate the time evolution of current vectors under clockwise inertial oscillations. The left column shows schematic vews of $\mathbf{u}$ at temporal intervals $\frac{n\pi}{2f}$ ($n = 0, 1, 2, \ldots$). Over this period, clockwise rotation of $\mathbf{u}$ by 90° fully transforms ζ into Γ, and Γ into $-\zeta$.

3.2 Relating upwelling and NIW generation to TC winds

When winds act on the ocean surface, momentum imparted by τ drives both mean and turbulent flows. Initially, $\overline{\mathbf{u}}$ accelerates in the direction of τ while turbulence helps distribute momentum vertically and deepen the ML. Later on, $\overline{\mathbf{u}}$ undergoes inertial rotation and becomes misaligned with τ. Variations in the alignment between τ and $\overline{\mathbf{u}}$ play a crucial role in setting the ocean response to TCs. The misalignment gives rise to an asymmetric distribution of ML energy around the TC track (Chang & Anthes, 1978) and can stop ML deepening by turbulence when $\overline{\mathbf{u}}$ approaches Ekman's balance and the rate of wind work $\tau \cdot \overline{\mathbf{u}}$ vanishes (Ekman, 1905; Pollard et al., 1973).

Setting $\nabla h = 0$ in equations (9)-(11), we may write the Ekman balance as $(\zeta, \Gamma) \sim \frac{1}{f\rho_0 h}(-\nabla\cdot\tau, \nabla\times\tau)$, so that Γ (and the resulting upwelling) is sustained by $\nabla\times\tau$. However, notice that $\nabla\times\tau$ does not directly drive the evolution of Γ in equation (10). Instead, $\frac{\partial\zeta}{\partial t}$ and $\frac{\partial\Gamma}{\partial t}$ at the initial stages of TC forcing will mirror patterns in $\nabla\times\tau$ and $\nabla\cdot\tau$ respectively. It is only later that the inertial rotation of currents gradually links $\nabla\times\tau$ to Γ and produces upwelling (Fig. 4).

The relative magnitudes of steady (Ekman) and oscillating (NIWs) components of the ocean response to TC forcing is mostly determined by U_{storm}, the horizontal scale of τ, and the group speed of mode-1 internal waves ($\|\mathbf{c_g^1}\|$). Using a two-layer model, Geisler (1970) showed that energy transfer into NIWs decreases with the ratio $U_{storm}/\|\mathbf{c_g}\|$, where $\|\mathbf{c_g}\|$ is the group speed of mode-1 internal waves. At the limit where $U_{storm}/\|\mathbf{c_g}\| < 1$, Geisler's solutions predict that the momentum in $\nabla\times\tau$ is entirely used by Ekman-style upwelling with no oscillatory behavior. Nilsson (1995) later generalized this result by deriving analytical expressions for the power put into geostrophic and NIW modes in a continuously stratified fluid given $\mathbf{c_g}$, U_{storm}, and the wavenumber spectrum of τ.

Super Typhoon Mangkhut had $U_{storm}/\mathbf{c_g} \sim 2$, indicating that the ocean response to its forcing may be expected to be dominated by NIWs rather than Ekman-style flows.

The formalism in equations (9)-(11) does not explicitly represent $\mathbf{c_g}$, but instead uses r to parameterize Eulerian momentum decay. Hence, we investigate whether this simple model of NIW generation can represent the transition between geostrophic and oscillatory regimes described by Geisler (1970) and Nilsson (1995). To do this, we used Euler's method to compute point solutions (setting $\nabla h = 0$) of equations (9)-(11) under the forcing of Gaussian vortices $\nabla \times \tau$ with standard deviations of 2 and 6 hours to represent fast- and slow-moving TCs respectively. These vortices represent the changing direction of tangential τ inside an axisymmetric TC eye but do not include radial stresses, which are known to make only minor contributions to NIW generation (Price, 1983; Shay et al., 1989; Nilsson, 1995). The evolution of $(\zeta/f, \Gamma/f, h)$ from an initial condition $(0, 0, 80$ m$)$ under both forcing scenarios and using $r = 0.2f$ is shown in Fig. 5.

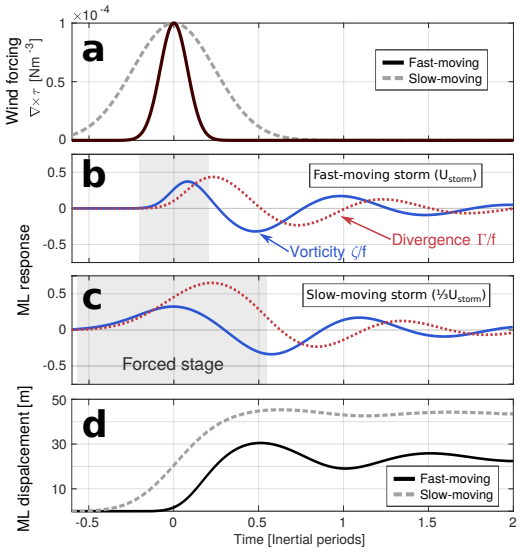

Figure 5. ML response (9)-(11) to (**a**) wind vortices representing (**b**) a fast-moving TC and (**c**) one moving at one-third the speed. (**d**) compares the mixed layer displacements $h(t_0) - h(t)$ that result from both simulations when $W_e = 0$ and $r = 0.2f$. Gray shading in (**b**) and (**c**) marks the forced stage, which is followed by near-inertial pumping as given by (12) and (13).

Numerical solutions of (9)-(11) in Fig. 5 exemplify the two fundamental differences noted by Geisler (1970). Firstly, notice that the greatest upwelling (maximum Γ/f) occurs at the end of the forced stage for the fast-moving case (Fig. 5b), whereas Γ/f peaks well within the slow TC's forced stage (Fig. 5c). Moreover, the net mixed layer displacement induced by the slow-moving TC is greater than for the fast-moving case (Fig. 5d).

The second point of agreement between our simple model and Geisler (1970) relates to the amplitude of NIWs generated by fast- and slow-moving TCs . While Geisler's analytical solutions to $\frac{\partial h}{\partial t}$ have no oscillatory behavior when $\frac{U_{storm}}{\mathbf{c}_g} < 1$, r regulates the fraction of momentum that enters the damped oscillator in equations (12) and (13) at the end of the forced stage. This is evidenced in Fig. 5 because the amplitude of NIWs generated by the slow-moving vortex is less than half that NIWs generated in fast-moving case (Fig. 5d and Figs. 3-5 in Geisler 1970).

The linear (ζ, Γ) view of ML dynamics (9)-(11) does not include any new physics absent from standard ocean models based on (u, v). Rather, it uses a simple change of

variables to explain inertial pumping (Fig. 4) using ordinary differential equations instead of partial ones, as done by Gill (1984). This helps conceptualize inertial pumping and upwelling as 1D (rather than 3D) processes. Furthermore, coupling between ζ and Γ concretely explains why NIW wakes are generally centered along the TC track where $\nabla\times\tau$ peaks and not on its right side, where the greatest concentration of near-inertial energy is (Price, 1981, 1983). Namely, NIWs only form where horizontal gradients (ζ and Γ) exist, and the forcing $\nabla\times\tau$ that directly drives cycles in ζ and Γ is greatest along the track. In the next section, we use float measurements and output from WRF-HYCOM coupled simulations of Mangkhut ($U_{storm}/\mathbf{c_g} \sim 2$) to demonstrate the relevance of (9)-(11) in describing NIW generation under fast-moving TCs.

4 Upper ocean dynamics beneath Mangkhut

We now turn our attention towards model output and observations of upper ocean dynamics beneath Super Typhoon Mangkhut. First, we present evidence supporting the validity of sampling and interpolation schemes described in Section 2. Second, the evolution of ζ and Γ, and their effect on T and S in our observations is explained using numerical solutions of equations (9)-(11). Altogether, these analyses exemplify and expand on the dynamics described in Section 3 and help visualize the mechanisms of NIW generation under fast-moving storms. The role of turbulent mixing in changing h is discussed briefly.

Mechanisms of NIW generation in model output and observations are compared (Fig. 6c) using a time series of the modelled $(\zeta,\Gamma)/f$ averaged between 14 and 14.5°N (solid lines) and float estimates ζ^*_{surf}/f along $y=0$ (dashed lines). Much like the idealized solutions in Figs. 4 and 5b, the ML response to Mangkhut can be described as a combination of initial forcing by $\nabla\times\tau$ and later coupling between ζ/f and Γ/f by inertial rotation of $\overline{\mathbf{u}}$. Atmospheric forcing is evidenced by a peak in ζ/f under the TC eye, while inertial rotation later transformed this response into a peak in Γ/f (Fig. 6c). As $\overline{\mathbf{u}}$ continued to rotate, ML flows reorganized to form minima in ζ/f and Γ/f along the TC track (Figs. 6a,b). At the end of the first inertial cycle, the ML came to have $\zeta/f \approx 0.25$ and $\Gamma/f \approx 0$ in both the 3D model and observations (Figs. 6c).

Broadly speaking, spatial patterns in $\|\overline{\mathbf{u}}\|$ and $(\zeta,\Gamma)/f$ in observations (Fig. 7) are consistent with those in the 3D model (Fig. 6a,b). Yet, some notable differences between the modelled and observed ML response exist. For example, $\Gamma^*_{surf}/f \sim 0.25$ near the leading edge of the TC eye (Fig. 7c), but the 3D model yields $\Gamma_{hycom}/f \sim -0.1$ there (Fig. 6b). Available data is insufficient to reliably attribute such differences to potential biases induced by windage and wave motion, our sampling and interpolation scheme, or to processes misrepresented in the 3D model. Nevertheless, patterns in $\mathbf{u}^*_{surf}$ and $\mathbf{u}^*_{mean}$ (Fig. 7a,b) are qualitatively similar to each other, suggesting that windage and wave motion only had a limited impact on $\mathbf{u}^*_{surf}$.

With the validity of our observational technique supported by model output, we now put our focus on the coupling between ζ/f and Γ/f and how it leads to NIW generation. To test whether observations are consistent with linear theory, Fig. 8 compares interpolated float data along $y=0$ to numerical solutions of equations (9)-(11) under idealized forcing and with a damping rate $r=0.5f$.

Atmospheric forcing $\nabla\times\tau$ in Fig. 8 corresponds to the reversal of tangential wind between opposite sides of the TC eyewall. The magnitude of $\nabla\times\tau$ used here agrees with the mean wind stress curl inside the TC eye ($\frac{|\tau_{\mathbf{max}}|}{\mathrm{MWR}} = 2.24\times10^{-4}$ N m^{-3}, dashed line), where $MWR = 40$ km is the radius of maximum wind and $|\tau_{max}| = C_D\rho_{air}|U_{10}|^2$ was calculated using $U_{10} = 70$ m s^{-1} (Fig. 1), $\rho_{air} = 1.22$ kg m^{-3}, and $C_D = 1.5\times10^{-3}$ (Zweers et al., 2010).

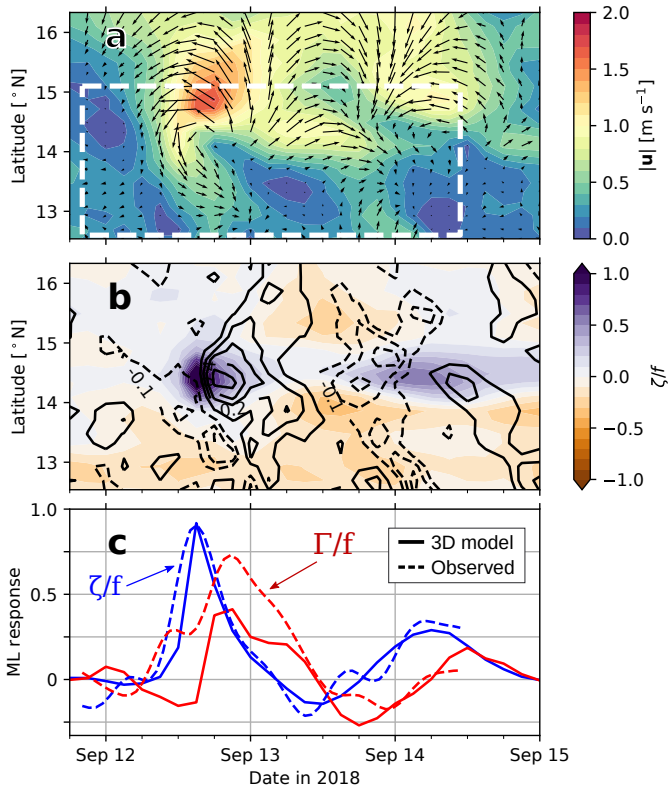

Figure 6. Hovmöller diagrams of the ML flow along 133 °E in terms of (**a**) $\bar{\mathbf{u}}$ and (**b**) $(\zeta, \Gamma)/f$ from the 3D coupled model, where black contours denote values $\Gamma/f = \pm 0.1, 0.2, \ldots$ (negative contours dashed). (**c**) Modelled $(\zeta, \Gamma)/f$ averaged between 14 and 14.5°N (solid lines) is compared to observed values along $y = 0$ (dashed lines). The dashed rectangle in panel **a** is representative of the area and stages of ocean response sampled by floats (Fig. 2b).

The magnitude of convergent stresses $\nabla \cdot \tau < 0$ is set to be artificially low in these simulations (Fig. 8a). Although $\|\nabla \cdot \tau\| \sim \|\nabla \times \tau\|$ in the 3D atmospheric model, the response in Γ that is generated by $\|\nabla \cdot \tau\|$ is rapidly suppressed by 3D and nonlinear effects and thus does not contribute significantly to NIW generation in the TC wake (Price, 1983; Shay et al., 1989). Lastly, it should be noted that forcing in Fig. 8a ignores the gradual weakening of τ far from the eyewall, where $\nabla \times \tau < 0$ and $\nabla \cdot \tau > 0$.

Agreement between linear solutions and observations in Fig. 8 confirms that clockwise rotation of $\bar{\mathbf{u}}$ (Fig. 2b) transformed the wind-forced ζ into Γ near the end of the forced stage. Momentum in Γ was later transferred to an inertial anticyclone $\zeta < 0$ and the cycle continued as shown schematically in Fig. 4. Note that the quality of the fit in Fig. 8b is sensitive to various model parameters (r, $\nabla \times \tau$, $\nabla \cdot \tau$), and initial conditions for (ζ, Γ, h). Nonetheless, this analysis confirms that ζ and Γ oscillate in quadrature in observations, the 3D model, and linear theory (Figs. 6c, 8b). This robust result comes from the linear terms by which f couples u and v in equations (6) and (**??**), and ζ and Γ in equations (9) and (10).

When Earth's rotation transferred ζ into Γ, the ML base moved upwards and a NIW was generated (Figs. 8c, 9a). Observations show that the 27°C isotherm deepened by ∼25 m under the TC eye before it shoaled by 75 m as predicted by linear theory (Fig. 8c). Initial deepening may be partially explained by turbulent mixing, evidenced by Thorpe

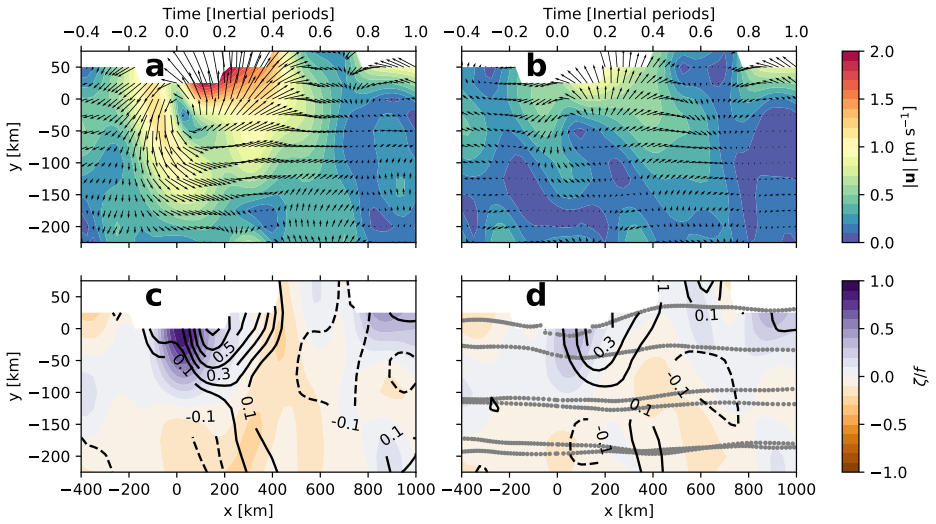

Figure 7. Observed ML dynamics under Mangkhut. (**a**) $\mathbf{u}^*_{surf}$ and (**b**) $\mathbf{u}^*_{mean}$ show current speeds in color shading. (**c**) ζ^*_{surf}/f and Γ^*_{surf}/f, and (**d**) ζ^*_{mean}/f and Γ^*_{mean}/f show the gradient-based description of ML motions. Black solid contours in Figs. 7c,d are for upwelling-favorable values $\Gamma/f > 0$, while dashed contours show $\Gamma/f < 0$. Dotted lines in Fig. 7d show float trajectories.

scale estimates $\kappa \sim 10^{-1}$ m^{2}s^{-1} near $x = 0$ km (Fig. 9b). Agreement between the modelled $\frac{\partial h}{\partial t}$ and observed displacements of the 27°C isotherm behind the TC are consistent with Γ^*_{surf} there (Fig. 8c). This result implies that upwelling in the wake of Mangkhut resulted from the near-inertial coupling of ζ and Γ, marking the generation of a large amplitude NIW. Moreover, the modelled Γ agrees well with Γ^*_{surf} for all $t > 0$ (Fig. 8b). However, Γ^*_{surf} failed to capture downwelling necessary to displace h after $t \approx 0.6$ inertial periods (Fig. 8c).

Profiles of w^* and u^* in Fig. 9a reveal the structure of upwelling in the wake of Mangkhut. There, w^* reaches 8 m h^{-1} and explains isothermal displacements as large as 75 m around $x = 350$ km. T^* shows that isotherms had been lifted by ~ 20 m after $\sim$0.85 inertial periods ($x = 850$ km, Fig. 9a). This net upwelling is crucial to the process of geostrophic adjustment (Geisler, 1970; Nilsson, 1995), and determined in (10)-(11) by the magnitude of r.

To test the impacts of advection in setting the ocean stratification behind Mangkhut, as well as the accuracy of inferred 3D flows (Eqs. 1-3), the Eulerian heating rate $\frac{\partial H_c}{\partial t} = \rho_0 C_p \frac{\partial T^*}{\partial t}$ is calculated along $y = 0$ through two different methods (Fig. 9b). First, we used a frozen field assumption so that $\frac{\partial T^*}{\partial t} = U_{storm} \frac{\partial T^*}{\partial x}$ (color shading). Second, we used $\mathbf{u}^*$ and w^* to calculate the advective contribution $\frac{\partial T^*}{\partial t} \approx -u^* \frac{\partial T^*}{\partial x} - v^* \frac{\partial T^*}{\partial y} - w^* \frac{\partial T^*}{\partial z}$ (black contours). Note that the latter expression ignores heating by turbulent mixing, while the frozen field estimate accounts for all observed heat transfer.

Areas of agreement between both estimates of $\frac{\partial H_c}{\partial t}$ (color shading and black contours in Fig. 9b) suggest that heat transfer was locally dominated by the vertical advection term $w^* \frac{\partial T^*}{\partial z}$ and that the approximation w^* is adequate. Similarities are particularly good near $x = 180$ km, where upwelling caused $\frac{\partial H_c}{\partial t} \sim$ -500 W m^{-3}.

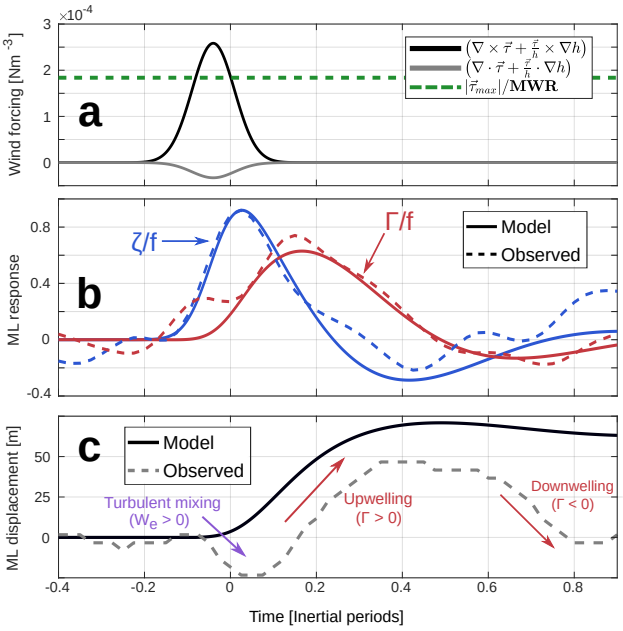

Figure 8. ML response to idealized TC-like atmospheric forcing. (**a**) Idealized wind forcing (solid lines) used to drive the ML linear model in equations (9)- (11) setting $W_e = \nabla h = 0$ and $r = 0.5f$. The dashed green line indicates the mean wind stress curl $\|\tau_{max}\|/MWR$ of the TC eye. (**b**) Numerical solutions of ζ/f (blue) and Γ/f (red) are compared to observations ζ_{surf}/f and Γ_{surf}/f along $y = 0$ km (Fig. 7c). (**c**) Linear solutions of $h(t)$ (solid line) are compared to observed displacements of the 27°C isotherm (dashed line).

Advective estimates of $\frac{\partial H_c}{\partial t}$ mistakenly predict cooling below 75 m depth around $x = 0$, where T^* shows heating rates as high as 300 W m^{-3} (color shading). Disagreement between observed heating and advective estimates below the TC eye may be explained by a possible bias in Γ^*_{surf} (Fig. 6c) but also by vigorous mixing. Thorpe scale estimates $\kappa \sim 10^{-1}$ m^2 s^{-1} near $x = 0$ (Fig. 9b) reveal areas where the corresponding turbulent heat flux $J_q \sim 4000$ W m^{-2} could invalidate the assumption that $\frac{\partial H_c}{\partial t}$ was dominated by advection. This value of J_q is roughly 15 times greater than the mean daily shortwave flux across the air-sea interface, but transfers heat into the thermocline, which is usually not directly impacted by air-sea fluxes.

While variations in the ML flow are dominated by near-inertial oscillations (Fig. 8), $\frac{\partial H_c}{\partial t}$ also shows the signature of higher-frequency motions (Fig. 9b). Horizontal sections of $\zeta^*/f, \Gamma^*/f$, and $N^* = \sqrt{-\frac{g}{\rho_0}\frac{\partial \rho^*}{\partial z}}$ at 160 m depth (Fig. 10) feature nearly parallel, periodic stripes that move away from the storm track towards $y < 0$. Dashed black lines in Fig. 10 help identify this apparent propagation corresponding to a cross-track phase speed ~ 3.1 m s^{-1}. While ζ^*/f and Γ^*/f are linked by the rotation of current vectors (Fig. 4), Γ^* and N^* are linked by isopycnal displacement and straining. Therefore, these three variables offer complementary views of internal wave phase propagation.

Color shading in Fig. 10c shows the magnitude $\|\mathbf{u}^*_{surf} - \mathbf{u}^*_{mean}\|$ as a proxy for vertical shear below the ML. As evidence of shear instability, Thorpe scale estimates of ε are shown with colored circles (Fig. 10c). Both the greatest ε and the greatest density of overturns appear within 100 km of the TC eye. Ahead of Mangkhut, overturns

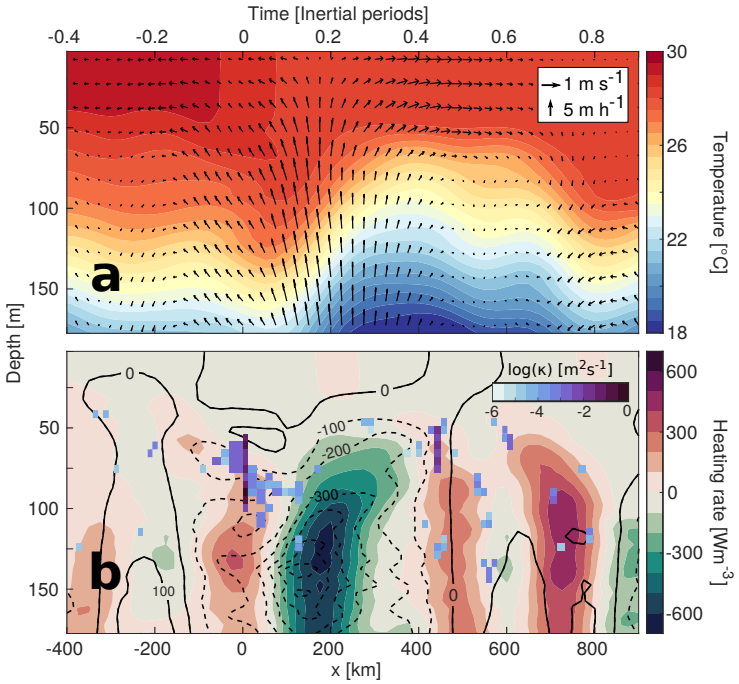

Figure 9. (**a**) Vertical sections of T^* and (u^*, w^*) along y=0 show the generation of a NIW behind Super Typhoon Mangkhut. The vertical component w^* is magnified for clarity. (**b**) Frozen field estimates (color shading) and advective contributions (black contours) to the Eulerian heating rate $\frac{\partial H_c}{\partial t}$, while estimates of κ indicate the intensity of vertical mixing inferred from Thorpe scales in M3 data (note the log scale).

with $\varepsilon < 10^{-7}$ W kg^{-1} were sampled at nearly equidistant locations by floats M3, M6, and M0. Conversely, overturns in the TC wake appeared more sporadically and clustered around a few locations, but with most values of ε ranging between $10^{-7.5}$ and 10^{-6} W kg^{-1}.

5 Upper ocean thermodynamics beneath Mangkhut

5.1 Mixed layer deepening and turbulent entrainment

Space-time variations in subsurface T and S result from 3D advection, mixing, and interactions with the atmosphere. In the case of intense, fast-moving TCs like Mangkhut ($U_{storm}/\mathbf{c_g} \sim 2$), shear-driven mixing at the ML base is expected to dominate upper ocean cooling (D'Asaro, 2003; Vincent et al., 2012). This process is evidenced by float measurements of T averaged between 0.5 and 1.5 m depth (Fig. 11a), which show a generalized cooling trend during TC passage.

In particular, 1-m binned profiles of T, S and potential density (σ_θ) from float M3 show a clear, gradual deepening of the ML base between $x = -250$ and $x = 0$ km (Figs. 11b-d). Successive float profiles made within $-250 < x < 0$ km (Figs. 11b-d) show decreases in SST but increases in both sea surface salinity (SSS) and σ_0 as the ML deepened. This corresponds to entrainment of cold, salty water from below and implies that a fraction of turbulent kinetic energy in wind-driven currents was used to raise the potential energy (PE) of the water column. In fact, density data (ρ) from floats M1 and

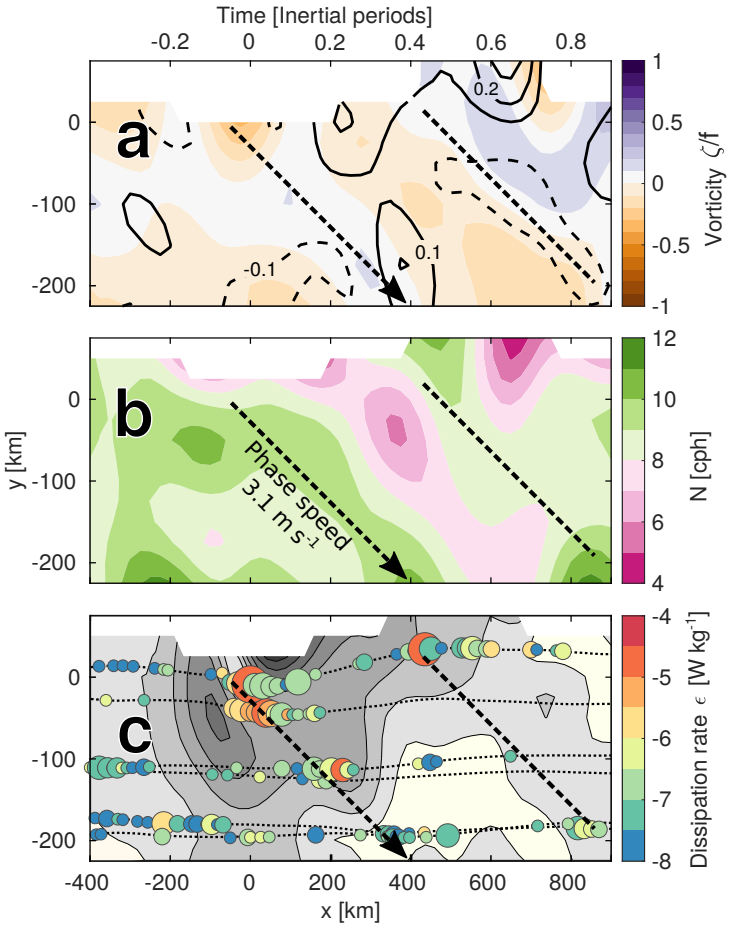

Figure 10. Horizontal sections of dynamical variables at 160 m depth. (**a**) ζ^* (color) and Γ^* (black contours, negative dashed), and (**b**) N^*. The color of circles in panel **c** indicate depth-averaged estimates of ε, while their size indicates the height of overturns (range is between 5 and 25 m). Gray shading in **c** shows $\|\mathbf{u}^*_{surf} - \mathbf{u}^*_{mean}\|$ as a proxy for vertical shear at the mixed layer base. Thin, dotted lines denote individual float tracks. Note that scales differ in x and y.

M3 indicate that $PE^0_{-60} = \int_{-60}^{0} \rho g z dz$ in the upper 60 m increased by $\sim$ 9 and 10 $\times$ 10^3 J m^{-2} between $x = -200$ and 200 km respectively.

As further evidence of the vigorous turbulence that transformed ocean thermodynamics beneath Mangkhut, vertical profiles of σ_0 feature $\sim$10 m-tall regions with unstable stratification (i.e. $\frac{\partial \sigma_0}{\partial z} > 0$, Fig. 11d). Thorpe scale estimates (see Section 2.2) in Figs. 9b and 10c indicate the contribution of these density overturns to ocean turbulence. Overall, these agree with the timing of ML deepening and SST cooling (Figs. 8c, 11a). Quantitatively, we estimate the turbulent heat flux $J_q \sim 4000$ W m^{-2} out of the ML for float M3 near $x = 0$ km (given $\kappa \sim 0.1$ m^2 s^{-1} and $\frac{\partial T}{\partial z} \sim 0.01$ °C m^{-1} in equation 5). For a ML with $h = 40$ m, this value of J_q corresponds to an SST cooling rate ~ -0.1 °C hr^{-1}, consistent with observations in Fig. 11a. The corresponding salinity flux $\kappa \frac{\partial S}{\partial z}$ is $\sim 1 \times 10^{-3}$ psu m s^{-1} out of the ML, equivalent to a rate of increase ~ 0.1 psu hr^{-1}, also consistent with observations by M3 (Fig. 12a).

After storm passage, SSS (SST) had increased (decreased) for all floats (Figs. 11a, 12a), indicating widespread mixing of the upper ocean beneath Mangkhut. In fact, plan

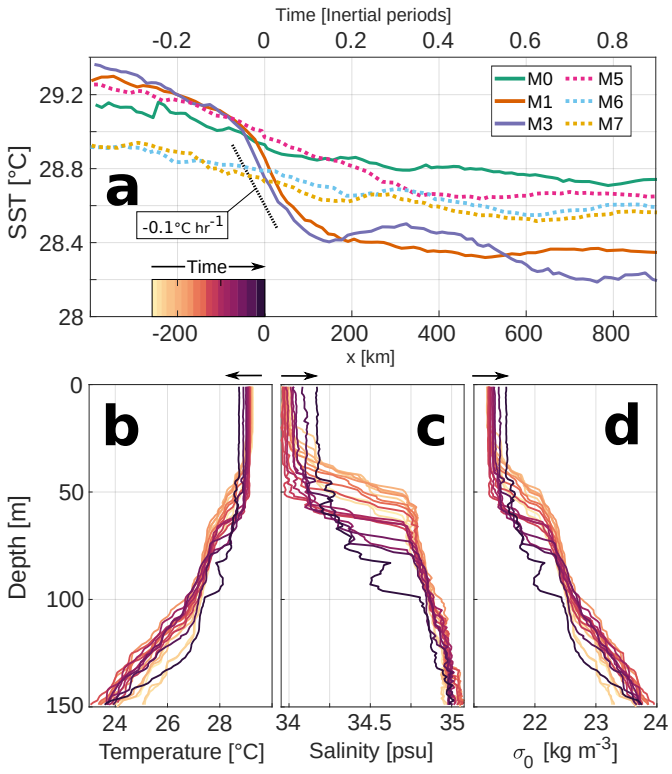

Figure 11. SST cooling by turbulent entrainment. (**a**) SST measured by all floats as a function of along-track distance x. 1-m binned profiles of (**b**) T, (**c**) S, and (**d**) potential density σ_0 measured by float M3 between $x = -250$ and $x = 0$. Individual profiles shown in the lower panels are color coded by their position in x (color bar in panel a).

views of near-surface $T^*(x, y)$ and $S^*(x, y)$ in Fig. 13 reveal a narrow and asymmetric wake of cold, salty water. This indicates that SST cooling was dominated by turbulent mixing and is consistent with greater windwork and current speeds for $y > 0$ (Figs. 6a, 7a,b, Chang & Anthes 1978; Price 1981). Furthermore, gradients $\frac{\partial T^*}{\partial x}$ and $\frac{\partial S^*}{\partial t}$ (not shown) indicate that maximum mixing rates occurred within 100 km of the TC eye, in agreement with Thorpe scale estimates in Figs. 9b and 10c.

The impact of precipitation on SSS is opposite to that of mixing and thus can be assessed from Fig. 12a, as floats M5, M6 and M7 sampled sharp decreases in SSS between $x = -250$ and $x = -150$ km. To examine the impacts of rainfall in near-surface T and S, we interpolated data from the Integrated Multi-Satellite Retrievals for Global Precipitation Measurement (IMERG, Huffman et al. (2015)) onto the times and locations of float measurements. Estimated hourly rates of precipitation (size of circles) and cumulative rainfall integrated since floats were at $x = -400$ km (color) show that all floats experienced considerable precipitation (Fig. 12b). However, and despite receiving more freshwater (~ 300 mm) than any other floats, time series of SSS from M1 and M3 do not feature noticeable decreases attributable to precipitation (Fig. 12).

Why is that so? In order for precipitation to impact SSS measurements, surface rain layers must form and remain stable for long enough (> 30 minutes) to be sampled by floats. However, this is only possible when buoyancy production by rainfall is greater than buoyancy mixing rates that diffuse salinity gradients (E. J. Thompson et al., 2019). Given that floats M1 and M3 were near the TC track and experienced the greatest tur-

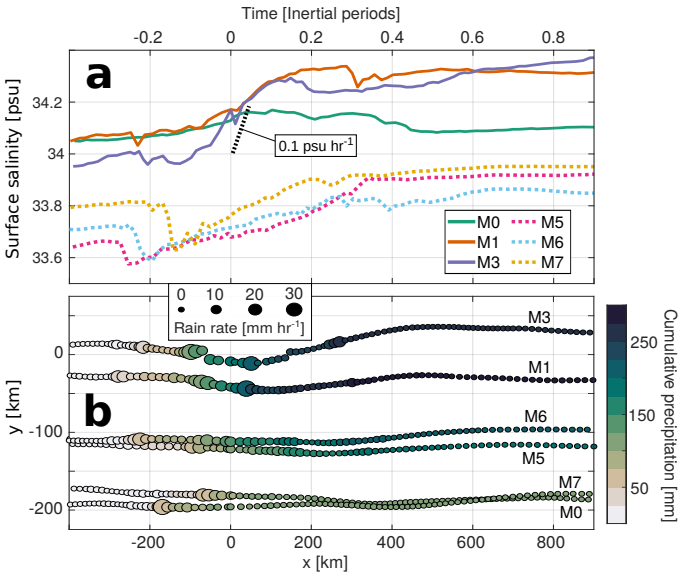

Figure 12. (**a**) S averaged in the upper 5 m along float tracks increases as a response to mixing of subsurface waters and decreases due to rainfall. (**b**) IMERG data show rain rates and cumulative precipitation along float trajectories.

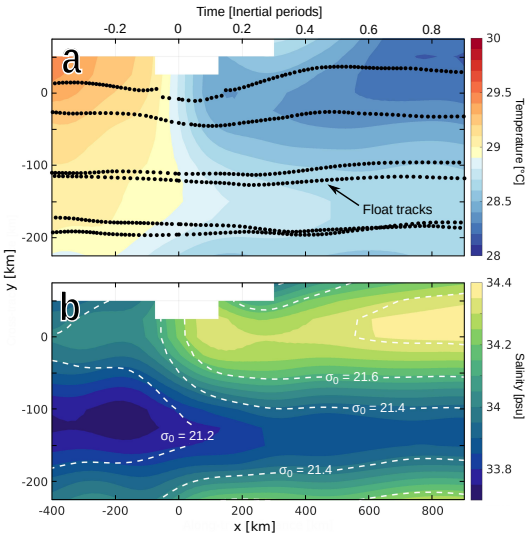

Figure 13. Plan view of (**a**) T^* and (**b**) S^* averaged over the upper 5 m. Black dots in Fig. 13a show the locations of each profile, while dashed contours in Fig. 13b show values of σ_θ in units of kg m^{-3}.

bulence rates (Fig. 10c), it is likely that sudden SSS freshening by rainfall was quickly mixed before it could be sampled.

In fact, successive profiles of T and S retrieved by float M7 (Fig. 14) detail the process of rain layer formation and their subsequent destruction by turbulent mixing. Each row of plots in this sequence shows 5 consecutive profiles spanning $\sim$ 3 h ($\sim$ 75 km). At the beginning, float profiles ranging from $x = -246$ to $x = -168$ km show a well-mixed upper ocean with no vertical gradients in T or S (Figs. 14a,b). Later on, a layer

of water with low T and S formed in the upper 5 m around $x = -140$ km (black line) but was gradually mixed and deepened over the following casts (Figs. 14c,d). This rain layer accounts for the sharp decrease in SSS measured by M7 (Fig. 12a), while the subsequent increase in SSS was consistent with mixing of cold, salty water from below. Roughly four hours (near $x = -50$ km) after its formation, there was little to no indication left that a rain layer had formed around float M7 (Figs. 14e,f).

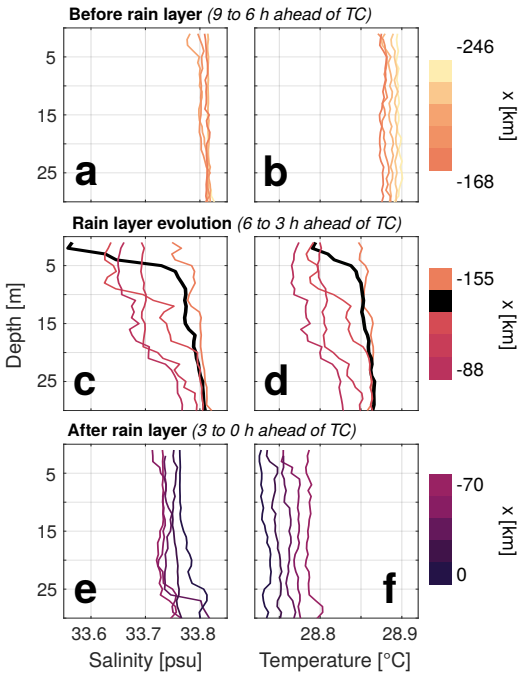

Figure 14. Three stages of rain layer evolution. Each row shows 5 consecutive profiles of T and S (color-coded by along-track position x) measured by float M7 over a ~ 3 h period. (**a**) S and (**b**) T before rainfall effects were noticeable. (**c**) and (**d**) show the formation of a rain layer (black line) and its gradual diffusion to greater depths. On Figs. 14e,f, turbulent mixing has mostly de-stratified the upper ocean.

Under fast-moving and high-intensity TCs like Mangkhut, precipitation can counteract some impacts of mixing, increasing S and decreasing σ_0 in the ML (Huang et al., 2009; Reul et al., 2021). Mixing a rain layer with $S = 0$ and thickness $\Delta h_{rain} = 0.3$ m (Fig. 12b) into a ML with $S = 34$ psu and $h = 40$ m would decrease SSS by 0.2 psu and surface σ_0 by 0.15 kg m^{-3}. This is equivalent to $\sim 60\%$ of the observed increase in SSS near the TC track (Fig. 12a) and $\sim 25\%$ of the observed change in surface σ_0 (Fig. 13b). In the case of Mangkhut, the SSS and surface σ_0 anomalies induced by rainfall were $\sim -30\%$ and $\sim -15\%$ as large as those caused by mixing.

As an indirect effect of precipitation on air-sea interaction under TCs, we now consider the energetics associated with rain layer destruction by mixing. To estimate this, we compare PE of a water column before and after buoyancy anomalies in a rain layer Δh_{rain} have been mixed down to the ML base. For $\Delta h_{rain} = 0.3$ m, PE in the upper 60 m changes by $\sim 10^3$ J m^{-2}, roughly 10% of the change estimated between $x = -200$ and $x = 200$ km for floats M1 and M3. This suggests that rain layer destruction can take up $\sim 10\%$ of turbulent kinetic energy under TCs, therefore inhibiting further SST cooling by mixing across the ML base (Jourdain et al., 2013).

5.2 Turbulent ocean heat pump

While the impacts of TC-driven turbulence are most noticeable in the formation of cold and salty wakes (Fig. 13), subsurface mixing helps regulate ocean heat uptake and transport (Sriver & Huber, 2007; Jansen et al., 2010; Mei et al., 2013). To assess these effects, modellers often make assumptions about the spatial and temporal extent of anomalous κ driven by TCs. Below, we analyze observed changes in the T-S relations to infer κ in the TC wake. In this way, we retrieve information about TC-driven mixing that may not be inferred from surface or ML thermodynamics alone.

Changes in T-S relations for floats M1 and M3 (Fig. 15a) resulted from a combination of turbulence, 3D advection, and atmospheric fluxes. However, the effects of turbulence are distinguishable from others because mixing between two water masses produces a weighted average of their original T-S properties (Hautala et al., 1996; Alford et al., 1999; Moum et al., 2003). For example, Fig. 15b, shows the average T-S relations measured by float M3 within the ranges $200 \leq x \leq 400$ km and $400 \leq x \leq 600$ km (dashed and solid lines respectively).

To assess the role of turbulence in setting the evolution between the two T-S profiles in Fig. 15b, we compare observations to the evolution predicted by

$$\frac{\partial T}{\partial t} \sim \kappa \frac{\partial^2 T}{\partial z^2} \tag{14}$$

$$\frac{\partial S}{\partial t} \sim \kappa \frac{\partial^2 S}{\partial z^2}. \tag{15}$$

Equations (14) and (15) ignore the effects of 3D advection and air-sea interaction, and thus describe only the effects of mixing on T-S relations. Taking the profile observed by M3 for $x \in (200, 400)$ as our initial condition and setting $\kappa = 3 \times 10^{-3}$ and 1×10^{-2} m^2 s^{-1} over 8 h (0.2 inertial periods) yields the T-S profiles shown in black dashed lines (Fig. 15b). These solutions to equations (14) and (15) agree well with the observed T-S changes for $\sigma_\theta < 23.2$ kg m^{-3} but fail to explain observations at greater densities (Fig. 15b). More precisely, note that for $\sigma_\theta > 23.5$ kg m^{-3}, the observed S was beyond the range of S in the initial condition. Such a transformation requires input of high-S water from elsewhere and hence cannot result from vertical mixing. Altogether, these analyses suggest mixing dominated watermass transformations down to ~ 110 m depth between $x = 200$ and $x = 600$ km, while 3D advection had greater impacts below that.

Values $\kappa > 10^{-3}$ m^2 s^{-1} inferred from this analysis are 3-10 times greater than the majority of Thorpe scale estimates between $x = 200$ and 600 km, whose mean value is $7.1{\times}10^{-4}$ m^2 s^{-1} (Fig. 9b). However, these estimates are not contradictory, as ocean turbulence is highly intermittent and the effective κ over long periods of time (Fig. 15b) is disproportionately determined by few mixing events with high κ (Baker & Gibson, 1987; Pearson & Fox-Kemper, 2018; Cael & Mashayek, 2021). Therefore, estimates κ across individual mixing events (Fig. 9b) are expected to have lower magnitudes than bulk estimates of κ derived from analyses of water mass transformation (Fig. 15), which yield effective or time-averaged values of κ.

To assess the long-term impacts of 'residual' mixing in the TC wake (Fig. 15b), we use $\kappa = 3{-}10{\times}10^{-3}$ m^2 s^{-1} to compute J_q across the 26°C isotherm in T^*, yielding mean values $\langle J_q \rangle \approx 1900 \pm 1000$ W m^{-2} within $200 < x < 600$ km and $-50 < y < 50$ km. This value of is roughly three times as large as the downwelling shortwave radiative flux in this area, which peaks near 700 W m^{-2}. Given that SST cooling typically stops only a few hours after TC passage (Figs. 11a), it is often assumed that TC-driven mixing stops then too. Nevertheless, these measurements (Fig. 15b) indicate that the vertical redistribution of heat by TC-driven turbulence can last beyond what SST data

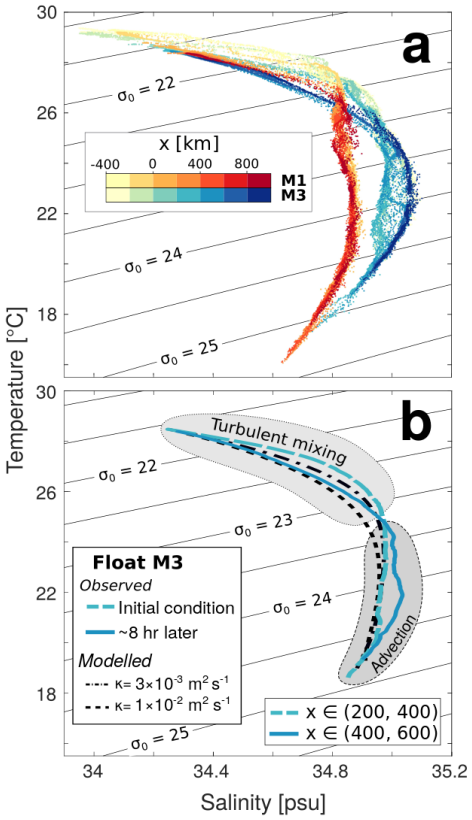

Figure 15. *T-S* profiles measured by floats M1 and M3 are color-coded by along-track distance in panel **a**. Mean profiles measured between 200 and 400 km (dashed line) and between 400 and 600 km (solid line) in **b** show transformations caused throughout an 8 h period. Black dashed lines show T-S properties modelled using (14) and (15) under the initial condition $x \in (200, 400)$km and different values of κ.

would suggest. The persistence and vertical distribution of heat content anomalies days to weeks after Mangkhut was studied by Johnston et al. (2020), who highlighted advection of subsurface anomalies by the North Equatorial Current and potential interactions with subsequent TCs.

6 Discussion

The 3D ocean response to Super Typhoon Mangkhut was reconstructed and diagnosed using data from profiling floats. We find general agreement between interpolated fields and a 3D model (Figs. 6, 7). A linear model using ζ and Γ instead of $\overline{\mathbf{u}}$ to describe ML dynamics helped interpret measurements and identify the mechanisms driving NIW generation (Figs. 8, 9). Lastly, estimates of κ and ε based on T and S data provides insight about the spatiotemporal persistence of TC-driven mixing and impacts to upper ocean thermodynamics (Figs. 9b, 10c, 14, 15b).

6.1 Linear ML dynamics and inertial pumping

Our analyses provide a simple, yet thorough description of the mechanism responsible for NIW generation by TCs because (a) for the first time, the dynamics of inertial

pumping are reduced to a set of ordinary differential equations (9)-(11) for ζ and Γ, and (b) observations of ζ and Γ were found to be in agreement with both linear theory and a 3D model (Figs. 6, 8). The theoretical and observational results of this study are in close alignment with early analyses by Geisler (1970) and Price (1981, 1983), meaning that we have not unveiled any new physics. Rather, the significance of this study is in pointing out the inertial coupling between ζ and Γ as the essence of inertial pumping and in using observations to convincingly show those physics at work under a TC of extreme intensity (Fig. 2c). Therefore, we hope that these analyses will be helpful to readers seeking to better understand the physics of NIW generation by moving storms and improve sampling strategies meant to observe these dynamics.

Past studies have inferred the 3D structure of upper ocean features powered by TCs (Price et al., 1994; Jacob et al., 2000; Sanabia & Jayne, 2020). Here, the (ζ, Γ) framework presented in Section 3 helped us to unambiguously relate observed isothermal displacements to TC forcing (Figs. 8, 9). This is result significant beyond the study of TCs because it demonstrates that equations (9)-(11) can relate storm morphology (represented by $\nabla \times \tau$ and $\nabla \cdot \tau$) to patterns in NIW generation in a 1D framework. While our results validate (9)-(11) in reproducing upwelling and NIW generation by fast-moving TCs, future studies may test it for slow-moving TCs and frontal storms in the mid latitudes, for which $\nabla \cdot \tau$ may play a crucial role (see for example Kundu & Thomson 1985). Furthermore, general nonlinear dynamical models based on ζ and Γ (see for example Névir & Sommer 2009) may facilitate further insight of internal waves generated by sources other than atmospheric forcing.

6.2 Float-based estimates of ζ and Γ

Float estimates of ζ and Γ are biased for $x > 500$ km, as they failed to capture $\Gamma < 0$ necessary for downwelling evidenced by T^* (Figs. 8c, 9). This is likely due to the loss of coherence by NIWs in the TC wake, since derivatives $\frac{\partial u^*}{\partial y}$ and $\frac{\partial v^*}{\partial y}$ are set by differences in measurements made more than 200 km and 12 hours apart (Figs. 1, 2). Time-dependent biases in $(\zeta^*_{surf}, \Gamma^*_{surf})/f$ affect the value $r = 0.5f$ used for numerical solutions in Fig. 8, which is considerably higher than values $\sim 0.2f$ commonly used to reproduce $\bar{\mathbf{u}}$ under extratropical storms (Pollard & Millard, 1970; D'Asaro, 1985; Alford, 2001). Past studies have argued that r is greater in TC wakes due to incraesed NIW energy flux divergence caused by the point-like nature of TC forcing (Kundu & Thomson, 1985) and interactions with background motions (Guan et al., 2014). However, aforementioned uncertainties in our estimates $(\zeta_{surf}, \Gamma_{surf})$ complicate interpretations of the significance of the value $r = 0.5f$ used here and its relation to NIW dynamics. A detailed analysis of NIW properties using this dataset over longer timescales is given by Johnston et al. (2021).

6.3 Float-based descriptions of mixing

Vertical profiles of T and S (Figs. 11, 14) detail mixing processes that modulate storm development. Thorpe scale estimates of κ and ε (Figs. 9, 10) provide the spatial distribution of mixing and potential impacts to air-sea interactions. While turbulent heat fluxes have been calculated directly using Lagrangian instruments (D'Asaro, 2003), the indirect approach followed here allows near real-time monitoring with potential applications in forecasting. Moreover, the watermass transformation analysis in Fig. 15 and inferred turbulent mean heat fluxes $J_q \approx 1900 \pm 1000$ W m^{-2} across the 26 °C in the TC wake show that subsurface redistribution of heat by mixing may persist after SST stabilizes. Following these examples, future experiments may use autonomous floats to track and explain heat anomalies induced by TCs (Johnston et al., 2020) aiming to improve parameterizations used in studies of TC-climate interaction (Sriver & Huber, 2007; Korty et al., 2008; Jansen et al., 2010).

7 Conclusions

Formulating the linear ML dynamics using ζ and Γ in equations (9)-(11) yields a direct statement of inertial pumping and explains NIW generation behind TCs. More precisely, this gradient-based view shows that the clockwise rotation of currents rearranges (u, v) so that ζ evolves into Γ, and Γ into $-\zeta$ (Fig. 4). In these cycles, ζ and Γ remain in quadrature as are u and v for NIWs. ML currents in observations and a 3D model of Mangkhut followed this pattern, which also controlled w in the TC wake (Figs. 6, 8).

Our analyses include multiple indirect descriptions of ocean mixing and its effects. Progressive changes in profiles of T and S indicate that SST cooling beneath Mangkhut was dominated by turbulent entrainment into the ML (Fig. 11, 13). Thorpe scale estimates in regions of unstable stratification suggest that active mixing happened ahead, under, and behind Mangkhut but was most vigorous near the TC eye (Fig. 10c), where we estimate $\kappa \sim 10^{-1}$ m^2 s^{-1}. This corresponds to heat fluxes of $\sim 4 \times 10^3$ W m^{-2} across the ML base (Figs. 9) and can explain the observed SST cooling rate ~ 0.1 °C hr^{-1} (Fig. 11a). Likewise, the corresponding salinity flux $\kappa \frac{\partial S}{\partial z} \sim 2 \times 10^{-3}$ psu m s^{-1} explains an increase of ~ 0.1 psu hr^{-1} in SSS, roughly the same as the greatest rates in our observations (Fig. 12a). Furthermore, our measurements highlight the effects of near-surface rain layers (Fig. 14), whose diffusion into the ML was estimated to take up $\sim 10\%$ of the turbulent kinetic energy budget near the TC track. Lastly, we documented the continued transformation of watermass characteristics hundreds of kilometers behind the TC with diffusivities $\kappa > 10^{-3}$ m^2 s^{-1} down to ~ 110 m depth (Fig. 15).

Insufficient spatial resolution in numerical models causes them to underestimate the intensity of TC winds (Walsh et al., 2007), subsequent upwelling, and NIW generation (Vincent et al., 2012). Likewise, it is unclear whether mixing parameterizations used by models can reproduce the full set of impacts reported here and others that may remain undetected. For example, accurate representation of mixing in rain layers (Fig. 14) and barrier layers (Balaguru et al., 2012; Rudzin et al., 2019) is challenging but necessary to avoid biases in forecasts of storm intensity (Hlywiak & Nolan, 2019). These and other intricacies associated with TC-driven mixing and NIW generation, including their long-term impacts on ocean thermodynamics, have yet to be comprehensively described in observations. Analyses presented in Sections 4 and 5 exemplify how data from autonomous platforms can provide insight about the multiscale ocean response to TCs. Such profiling float measurements are crucial to accurately constrain the role of TCs in global budgets of mixing and internal wave energy.

Acknowledgments

This work is supported by grant NA17OAR4310259 from the Climate Variability and Predictability program at NOAA, and grants N00014163085 and N000141613073 from the Office of Naval Research's PISTON initiative, which are components of the international Years of the Maritime Continent program. We are grateful to the master, crew, and science party on *R/V Thomas Thompson* for their help in deploying floats. The Instrument Development Group at the Scripps Institution of Oceanography designed, prepared, and monitored the SOLO-II floats. N.G.B. is funded by Consejo Nacional de Ciencia y Tecnología (CONACyT) and UC Mexus. E.J.T. contributes effort with funding from the NOAA Weather Program Office's Precipitation Prediction Grand Challenge. Kristin Zeiden, Nathalie Zilberman, William R. Young, and three anonymous reviewers provided valuable comments.

Float data are available at the PISTON data site www-air.larc.nasa.gov/cgi-bin/ArcView/camp2ex?TRAJECTORY=1#JOHNSTON. SHAUN. Tropical cyclone best track data are available from the JTWC at https://www.metoc.navy.mil/jtwc/jtwc.html?western-

pacific (Mangkhut was storm 26 of 2018) and coupled ocean-atmosphere model results are available at https://doi.org/10.5281/zenodo.4134671.

References

Alford, M. H. (2001). Internal swell generation: The spatial distribution of energy flux from the wind to mixed layer near-inertial motions. *Journal of Physical Oceanography*, *31*(8), 2359–2368. doi: https://doi.org/10.1175/1520-0485(2001)031⟨2359:ISGTSD⟩2.0.CO;2

Alford, M. H., & Gregg, M. C. (2001). Near-inertial mixing: Modulation of shear, strain and microstructure at low latitude. *Journal of Geophysical Research: Oceans*, *106*(C8), 16947–16968. doi: https://doi.org/10.1029/2000JC000370

Alford, M. H., Gregg, M. C., & Ilyas, M. (1999). Diapycnal mixing in the Banda Sea: Results of the first microstructure measurements in the Indonesian Throughflow. *Geophysical Research Letters*, *26*(17), 2741–2744. doi: https://doi.org/10.1029/1999GL002337

Asselin, O., & Young, W. R. (2020, 06). Penetration of Wind-Generated Near-Inertial Waves into a Turbulent Ocean. *Journal of Physical Oceanography*, *50*(6), 1699-1716. Retrieved from `https://doi.org/10.1175/JPO-D-19-0319.1` doi: https://doi.org/10.1175/JPO-D-19-0319.1

Baker, M. A., & Gibson, C. H. (1987). Sampling turbulence in the stratified ocean: Statistical consequences of strong intermittency. *Journal of Physical Oceanography*, *17*(10), 1817–1836. doi: https://doi.org/10.1175/1520-0485(1987)017⟨1817:STITSO⟩2.0.CO;2

Balaguru, K., Chang, P., Saravanan, R., Leung, L. R., Xu, Z., Li, M., & Hsieh, J.-S. (2012). Ocean barrier layers' effect on tropical cyclone intensification. *Proceedings of the National Academy of Sciences*, *109*(36), 14343–14347. doi: https://doi.org/10.1073/pnas.1201364109

Balmforth, N., Llewellyn Smith, S. G., & Young, W. (1998). Enhanced dispersion of near-inertial waves in an idealized geostrophic flow. *Journal of marine research*, *56*(1), 1–40. doi: https://doi.org/10.1357/002224098321836091

Cael, B., & Mashayek, A. (2021). Log-skew-normality of ocean turbulence. *Physical Review Letters*, *126*(22), 224502. doi: https://doi.org/10.1103/PhysRevLett.126.224502

Chang, S. W., & Anthes, R. A. (1978). Numerical simulations of the ocean's nonlinear, baroclinic response to translating hurricanes. *Journal of Physical Oceanography*, *8*(3), 468–480. doi: https://doi.org/10.1175/1520-0485(1978)008⟨0468:NSOTON⟩2.0.CO;2

Chen, S. S., & Curcic, M. (2016). Ocean surface waves in Hurricane Ike (2008) and Superstorm Sandy (2012): Coupled model predictions and observations. *Ocean Modelling*, *103*, 161–176. doi: https://doi.org/10.1016/j.ocemod.2015.08.005

D'Asaro, E. A. (1985). The energy flux from the wind to near-inertial motions in the surface mixed layer. *Journal of Physical Oceanography*, *15*(8), 1043–1059. doi: https://doi.org/10.1175/1520-0485(1985)015⟨1043:TEFFTW⟩2.0.CO;2

D'Asaro, E. A. (1989). The decay of wind-forced mixed layer inertial oscillations due to the β effect. *Journal of Geophysical Research: Oceans*, *94*(C2), 2045–2056. doi: https://doi.org/10.1029/JC094iC02p02045

D'Asaro, E. A. (2003). The ocean boundary layer below Hurricane Dennis. *Journal of Physical Oceanography*, *33*(3), 561–579. doi: https://doi.org/10.1175/1520-0485(2003)033⟨0561:TOBLBH⟩2.0.CO;2

D'Asaro, E. A., Eriksen, C. C., Levine, M. D., Paulson, C. A., Niiler, P., & Van Meurs, P. (1995). Upper-ocean inertial currents forced by a strong storm. Part I: Data and comparisons with linear theory. *Journal of Physical Oceanography*, *25*(11), 2909–2936. doi: https://doi.org/10.1175/1520-0485(1995)025⟨2909:

753 UOICFB⟩2.0.CO;2
754 D'Asaro, E. A., Sanford, T. B., Niiler, P. P., & Terrill, E. J. (2007). Cold wake of
755 hurricane Frances. *Geophysical Research Letters*, *34*(15). doi: https://doi.org/10
756 .1029/2007GL030160
757 Davis, R. E. (1985). Objective mapping by least squares fitting. *Journal of*
758 *Geophysical Research: Oceans*, *90*(C3), 4773–4777. doi: https://doi.org/10.1029/
759 JC090iC03p04773
760 Davis, R. E., Sherman, J., & Dufour, J. (2001). Profiling ALACEs and other ad-
761 vances in autonomous subsurface floats. *Journal of atmospheric and oceanic tech-*
762 *nology*, *18*(6), 982–993. doi: https://doi.org/10.1175/1520-0426(2001)018⟨0982:
763 PAAOAI⟩2.0.CO;2
764 Ekman, V. W. (1905). On the influence of the earth's rotation on ocean-currents.
765 Emanuel, K. A. (1999). Thermodynamic control of hurricane intensity. *Nature*,
766 *401*(6754), 665–669. doi: https://doi.org/10.1038/44326
767 Emanuel, K. A. (2005). Increasing destructiveness of tropical cyclones over the past
768 30 years. *Nature*, *436*(7051), 686–688. doi: https://doi.org/10.1038/nature03906
769 Geisler, J. E. (1970). Linear theory of the response of a two layer ocean to a moving
770 hurricane. *Geophysical and Astrophysical Fluid Dynamics*, *1*(1-2), 249–272. doi:
771 https://doi.org/10.1080/03091927009365774
772 Gill, A. (1984). On the behavior of internal waves in the wakes of storms. *Jour-*
773 *nal of Physical Oceanography*, *14*(7), 1129–1151. doi: https://doi.org/10.1175/
774 1520-0485(1984)014⟨1129:OTBOIW⟩2.0.CO;2
775 Glenn, S., Miles, T., Seroka, G., Xu, Y., Forney, R., Yu, F., ... Kohut, J. (2016).
776 Stratified coastal ocean interactions with tropical cyclones. *Nature Communica-*
777 *tions*, *7*(1), 1–10. doi: https://doi.org/10.1038/ncomms10887
778 Guan, S., Zhao, W., Huthnance, J., Tian, J., & Wang, J. (2014). Observed upper
779 ocean response to typhoon Megi (2010) in the Northern South China Sea. *Jour-*
780 *nal of Geophysical Research: Oceans*, *119*(5), 3134–3157. doi: https://doi.org/10
781 .1002/2013JC009661
782 Hautala, S. L., Reid, J. L., & Bray, N. (1996). The distribution and mixing of
783 Pacific water masses in the Indonesian Seas. *Journal of Geophysical Research:*
784 *Oceans*, *101*(C5), 12375–12389. doi: https://doi.org/10.1029/96JC00037
785 Hlywiak, J., & Nolan, D. S. (2019). The influence of oceanic barrier layers on
786 tropical cyclone intensity as determined through idealized, coupled numer-
787 ical simulations. *Journal of Physical Oceanography*, *49*(7), 1723–1745. doi:
788 https://doi.org/10.1175/JPO-D-18-0267.1
789 Huang, P., Sanford, T. B., & Imberger, J. (2009). Heat and turbulent kinetic
790 energy budgets for surface layer cooling induced by the passage of Hurricane
791 Frances (2004). *Journal of Geophysical Research: Oceans*, *114*(C12). doi:
792 https://doi.org/10.1029/2009JC005603
793 Huffman, G. J., Bolvin, D. T., Braithwaite, D., Hsu, K., Joyce, R., Xie, P., & Yoo,
794 S.-H. (2015). NASA global precipitation measurement (GPM) integrated multi-
795 satellite retrievals for GPM (IMERG). *Algorithm Theoretical Basis Document*
796 *(ATBD) Version*, *4*, 26.
797 Hughes, K. G., Moum, J. N., & Shroyer, E. L. (2020). Evolution of the velocity
798 structure in the diurnal warm layer. *Journal of Physical Oceanography*, *50*(3),
799 615–631. doi: https://doi.org/10.1175/JPO-D-19-0207.1
800 Jacob, S. D., Shay, L. K., Mariano, A. J., & Black, P. G. (2000). The 3D oceanic
801 mixed layer response to Hurricane Gilbert. *Journal of Physical Oceanogra-*
802 *phy*, *30*(6), 1407–1429. doi: https://doi.org/10.1175/1520-0485(2000)030⟨1407:
803 TOMLRT⟩2.0.CO;2
804 Jansen, M. F., Ferrari, R., & Mooring, T. A. (2010). Seasonal versus permanent
805 thermocline warming by tropical cyclones. *Geophysical Research Letters*, *37*(3).
806 doi: https://doi.org/10.1029/2009GL041808

Johnson, H. L., & Garrett, C. (2004). Effects of noise on thorpe scales and run lengths. *Journal of physical oceanography*, *34*(11), 2359–2372. doi: https://doi.org/10.1175/JPO3021.1

Johnston, T. M. S., Chaudhuri, D., Mathur, M., Rudnick, D. L., Sengupta, D., Simmons, H. L., ... Venkatesan, R. (2016). Decay mechanisms of near-inertial mixed layer oscillations in the Bay of Bengal. *Oceanography*, *29*(2), 180–191. doi: https://doi.org/10.5670/oceanog.2016.50

Johnston, T. M. S., & Rudnick, D. L. (2009). Observations of the transition layer. *Journal of Physical Oceanography*, *39*(3), 780–797. doi: https://doi.org/10.1175/2008JPO3824.1

Johnston, T. M. S., Rudnick, D. L., Brizuela, N., & Moum, J. N. (2020). Advection by the North Equatorial Current of a cold wake due to multiple typhoons in the western Pacific: Measurements from a profiling float array. *Journal of Geophysical Research: Oceans*, *125*(4), e2019JC015534. doi: https://doi.org/10.1029/2019JC015534

Johnston, T. M. S., Wang, S., Lee, C.-Y., Moum, J. N., Rudnick, D. L., & Sobel, A. (2021). Near-inertial wave propagation in the wake of Super Typhoon Mangkhut: Measurements from a profiling float array. *Journal of Geophysical Research: Oceans*, e2020JC016749. doi: https://doi.org/10.1029/2020JC016749

Jourdain, N. C., Lengaigne, M., Vialard, J., Madec, G., Menkès, C. E., Vincent, E. M., ... Barnier, B. (2013). Observation-based estimates of surface cooling inhibition by heavy rainfall under tropical cyclones. *Journal of Physical Oceanography*, *43*(1), 205–221. doi: https://doi.org/10.1175/JPO-D-12-085.1

Korty, R. L., Emanuel, K. A., & Scott, J. R. (2008). Tropical cyclone–induced upper-ocean mixing and climate: Application to equable climates. *Journal of Climate*, *21*(4), 638–654. doi: https://doi.org/10.1175/2007JCLI1659.1

Kundu, P. K., & Thomson, R. E. (1985). Inertial oscillations due to a moving front. *Journal of Physical Oceanography*, *15*(8), 1076–1084. doi: https://doi.org/10.1175/1520-0485(1985)015⟨1076:IODTAM⟩2.0.CO;2

Kunze, E. (1985). Near-inertial wave propagation in geostrophic shear. *Journal of Physical Oceanography*, *15*(5), 544–565. doi: https://doi.org/10.1175/1520-0485(1985)015⟨0544:NIWPIG⟩2.0.CO;2

Le Traon, P., Nadal, F., & Ducet, N. (1998). An improved mapping method of multisatellite altimeter data. *Journal of atmospheric and oceanic technology*, *15*(2), 522–534. doi: https://doi.org/10.1175/1520-0426(1998)015⟨0522:AIMMOM⟩2.0.CO;2

Mater, B. D., Venayagamoorthy, S. K., St. Laurent, L., & Moum, J. N. (2015). Biases in Thorpe-scale estimates of turbulence dissipation. Part I: Assessments from large-scale overturns in oceanographic data. *Journal of Physical Oceanography*, *45*(10), 2497–2521. doi: https://doi.org/10.1175/JPO-D-14-0128.1

Mei, W., Primeau, F., McWilliams, J. C., & Pasquero, C. (2013). Sea surface height evidence for long-term warming effects of tropical cyclones on the ocean. *Proceedings of the National Academy of Sciences*, *110*(38), 15207–15210. doi: https://doi.org/10.1073/pnas.1306753110

Moum, J., Farmer, D., Smyth, W., Armi, L., & Vagle, S. (2003). Structure and generation of turbulence at interfaces strained by internal solitary waves propagating shoreward over the continental shelf. *Journal of Physical Oceanography*, *33*(10), 2093–2112. doi: https://doi.org/10.1175/1520-0485(2003)033⟨2093:SAGOTA⟩2.0.CO;2

Nagai, T., Tandon, A., Kunze, E., & Mahadevan, A. (2015). Spontaneous generation of near-inertial waves by the Kuroshio Front. *Journal of Physical Oceanography*, *45*(9), 2381–2406. doi: https://doi.org/10.1175/JPO-D-14-0086.1

Névir, P., & Sommer, M. (2009). Energy–vorticity theory of ideal fluid mechanics. *Journal of the Atmospheric Sciences*, *66*(7), 2073–2084. doi: https://doi.org/

10.1175/2008JAS2897.1

Nilsson, J. (1995, 04). Energy flux from traveling hurricanes to the oceanic internal wave field. *Journal of Physical Oceanography*, *25*(4), 558-573. doi: https://doi.org/10.1175/1520-0485(1995)025⟨0558:EFFTHT⟩2.0.CO;2

Osborn, T. (1980). Estimates of the local rate of vertical diffusion from dissipation measurements. *Journal of physical oceanography*, *10*(1), 83–89. doi: https://doi.org/10.1175/1520-0485(1980)010⟨0083:EOTLRO⟩2.0.CO;2

Pearson, B., & Fox-Kemper, B. (2018). Log-normal turbulence dissipation in global ocean models. *Physical review letters*, *120*(9), 094501. doi: https://doi.org/10.1103/PhysRevLett.120.094501

Pollard, R. T., & Millard, R. (1970). Comparison between observed and simulated wind-generated inertial oscillations. In *Deep sea research and oceanographic abstracts* (Vol. 17, pp. 813–821). doi: https://doi.org/10.1016/0011-7471(70)90043-4

Pollard, R. T., Rhines, P. B., & Thompson, R. O. (1973). The deepening of the wind-mixed layer. *Geophysical Fluid Dynamics*, *4*(4), 381–404. doi: https://doi.org/10.1080/03091927208236105

Price, J. F. (1981). Upper ocean response to a hurricane. *Journal of Physical Oceanography*, *11*(2), 153–175. doi: https://doi.org/10.1175/1520-0485(1981)011⟨0153:UORTAH⟩2.0.CO;2

Price, J. F. (1983). Internal wave wake of a moving storm. Part I. Scales, energy budget and observations. *Journal of Physical Oceanography*, *13*(6), 949–965. doi: https://doi.org/10.1175/1520-0485(1983)013⟨0949:IWWOAM⟩2.0.CO;2

Price, J. F., Sanford, T. B., & Forristall, G. Z. (1994). Forced stage response to a moving hurricane. *Journal of Physical Oceanography*, *24*(2), 233–260. doi: https://doi.org/10.1175/1520-0485(1994)024⟨0233:FSRTAM⟩2.0.CO;2

Reul, N., Chapron, B., Grodsky, S. A., Guimbard, S., Kudryavtsev, V., Foltz, G. R., & Balaguru, K. (2021). Satellite observations of the sea surface salinity response to tropical cyclones. *Geophysical research letters*, *48*(1), e2020GL091478. doi: https://doi.org/10.1029/2020GL091478

Rudzin, J. E., Shay, L. K., & Jaimes de la Cruz, B. (2019). The impact of the Amazon–Orinoco River plume on enthalpy flux and air–sea interaction within Caribbean Sea tropical cyclones. *Monthly Weather Review*, *147*(3), 931–950. doi: https://doi.org/10.1175/MWR-D-18-0295.1

Sanabia, E. R., & Jayne, S. R. (2020). Ocean observations under two major hurricanes: Evolution of the response across the storm wakes. *AGU Advances*, *1*(3), e2019AV000161. doi: https://doi.org/10.1029/2019AV000161

Sanford, T. B., Price, J. F., & Girton, J. B. (2011). Upper-ocean response to Hurricane Frances (2004) observed by profiling EM-APEX floats. *Journal of Physical Oceanography*, *41*(6), 1041–1056. doi: https://doi.org/10.1175/2010JPO4313.1

Scotti, A. (2015). Biases in Thorpe-scale estimates of turbulence dissipation. Part II: Energetics arguments and turbulence simulations. *Journal of Physical Oceanography*, *45*(10), 2522–2543. doi: https://doi.org/10.1175/JPO-D-14-0092.1

Shay, L. K., & Chang, S. W. (1997). Free surface effects on the near-inertial ocean current response to a hurricane: A revisit. *Journal of Physical Oceanography*, *27*(1), 23–39. doi: https://doi.org/10.1175/1520-0485(1990)020⟨1405:FSEOTN⟩2.0.CO;2

Shay, L. K., Elsberry, R. L., & Black, P. G. (1989). Vertical structure of the ocean current response to a hurricane. *Journal of Physical Oceanography*, *19*(5), 649–669. doi: https://doi.org/10.1175/1520-0485(1989)019⟨0649:VSOTOC⟩2.0.CO;2

Skamarock, W. C., Klemp, J. B., Dudhia, J., Gill, D. O., Barker, D. M., Wang, W., & Powers, J. G. (2008). A description of the Advanced Research WRF version 3. NCAR Technical note-475+ STR.

Sriver, R. L., & Huber, M. (2007). Observational evidence for an ocean heat pump

induced by tropical cyclones. *Nature*, *447*(7144), 577–580. doi: https://doi.org/10.1038/nature05785

Thomas, L. N., Rainville, L., Asselin, O., Young, W. R., Girton, J., Whalen, C. B., ... Hormann, V. (2020). Direct observations of near-inertial wave ζ-refraction in a dipole vortex. *Geophysical Research Letters*, *47*(21), e2020GL090375. doi: https://doi.org/10.1029/2020GL090375

Thompson, A., Gille, S. T., MacKinnon, J. A., & Sprintall, J. (2007). Spatial and temporal patterns of small-scale mixing in Drake Passage. *Journal of Physical Oceanography*, *37*(3), 572–592. doi: https://doi.org/10.1175/JPO3021.1

Thompson, E. J., Moum, J. N., Fairall, C. W., & Rutledge, S. A. (2019). Wind limits on rain layers and diurnal warm layers. *Journal of Geophysical Research: Oceans*, *124*(2), 897–924. doi: https://doi.org/10.1029/2018JC014130

Thorpe, S. (1977). Turbulence and mixing in a Scottish loch. *Philosophical Transactions of the Royal Society of London. Series A, Mathematical and Physical Sciences*, *286*(1334), 125–181. doi: https://doi.org/10.1098/rsta.1977.0112

Turner, J., & Kraus, E. (1967). A one-dimensional model of the seasonal thermocline i. a laboratory experiment and its interpretation. *Tellus*, *19*(1), 88–97. doi: https://doi.org/10.1111/j.2153-3490.1967.tb01461.x

Vincent, E. M., Lengaigne, M., Madec, G., Vialard, J., Samson, G., Jourdain, N. C., ... Jullien, S. (2012). Processes setting the characteristics of sea surface cooling induced by tropical cyclones. *Journal of Geophysical Research: Oceans*, *117*(C2). doi: https://doi.org/10.1029/2011JC007396

Wallcraft, A., Metzger, E., & Carroll, S. (2009). *Software design description for the hybrid coordinate ocean model (HYCOM), Version 2.2* (Tech. Rep.). Naval Research Lan Stennis Space Center MS Oceanography Div.

Walsh, K., Fiorino, M., Landsea, C., & McInnes, K. (2007). Objectively determined resolution-dependent threshold criteria for the detection of tropical cyclones in climate models and reanalyses. *Journal of Climate*, *20*(10), 2307–2314. doi: https://doi.org/10.1175/JCLI4074.1

Wamsley, L. (2018, Sep). Dozens more feared dead in the philippines after typhoon triggers mudslide. *National Public Radio*. Retrieved from `https://www.npr.org/2018/09/17/648866035/dozens-more-feared-dead-in-the-philippines-after-typhoon-triggers-mudslide`

Whitt, D. B., & Thomas, L. N. (2015). Resonant generation and energetics of wind-forced near-inertial motions in a geostrophic flow. *Journal of Physical Oceanography*, *45*(1), 181–208. doi: https://doi.org/10.1175/JPO-D-14-0168.1

Zweers, N., Makin, V., De Vries, J., & Burgers, G. (2010). A sea drag relation for hurricane wind speeds. *Geophysical Research Letters*, *37*(21). doi: https://doi.org/10.1029/2010GL045002